ADVANCED OPTICAL MATERIALS
www.advopticalmat.de

High-Q Plasmonic Resonances: Fundamentals and Applications

Baoqing Wang, Peng Yu, Wenhao Wang, Xutao Zhang, Hao-Chung Kuo, Hongxing Xu, and Zhiming M. Wang**

Subwavelength confinement of light with plasmonics is promising for nanophotonics and optoelectronics. However, it is nontrivial to obtain narrow plasmonic resonances due to the intrinsically high optical losses and radiative damping in metallic structures. In this review, a thorough summary of the recent research progress on achieving high-quality (high-Q) factor plasmonic resonances is provided, emphasizing the fundamentals and six resonant mode types, including surface lattice resonances, multipolar resonances, plasmonic Fano resonances, plasmon-induced transparency, guided-mode resonances, and Tamm plasmon resonances. The applications of high-Q plasmonic resonances in spectrally selective thermal emission, sensing, single-photon emission, filtering, and band-edge lasing are also discussed.

1. Introduction

Surface plasmon resonances (SPRs), a collective oscillation of free electrons in metallic nanostructures excited by the corresponding resonant wavelength of light, have attracted extensive attention due to their potential to circumvent the diffraction limit of conventional optics and enhanced light-matter interactions.[1] These unique properties empower transformation and manipulation of photonics, electronics, and nanotechnology, such as quantum optics,[2] nonlinear optics,[3] photodetection,[4] nanolensing,[5] sensing,[6] plasmon-controlled fluorescence,[7] photocatalysis,[8] circuits and devices,[9] and photovoltaics,[10] etc. Plasmon modes can be generally divided into propagating surface plasmons (PSPs) and localized surface plasmons (LSPs).[11] PSPs can be excited on extended metal surfaces by prism coupling or grating coupling, but it cannot be excited directly by the incident photon. LSPs are nonpropagating excitations of electrons in metallic nanostructures, and it can be excited directly by incident photons as momentum matching is not a requirement for their excitation because blending the relevant systems with metallic nanostructures breaks translational symmetry.[12] Although there are some differences between them, there is no clear boundary.[13]

However, in the past decades, the only widespread practical applications of plasmonics are surface-enhanced Raman scattering (SERS) and biochemical sensing because the loss is not a key factor for consideration.[14] Unfortunately, many other plasmonic devices are plagued by losses, such as metamaterials, superlenses, solar cells, plasmonic waveguides, color filters, etc., due to the nonradiative nature of plasmonic processes. Plasmonic devices generally require metallic materials. While offering extreme light confinements with ultrasmall mode volume, current plasmonic devices face significant challenges due to their losses encountered in the metallic components with a high concentration of free electrons. These free electrons exist in the materials that have negative real permittivity, and it is the essential property of any plasmonic materials. In general, the losses originate from interband and intraband transitions in the visible and infrared regions, respectively.

The spectral width and strength of the SPRs, characterized by full-width at half-maximum (FWHM) in transmission, absorption, reflection, extinction, can be evaluated by the quality factor (Q-factor). The losses in plasmonics can be characterized by evaluating the Q-factor, which is intrinsically linked to the ratio of energy stored to the energy lost by an oscillator.[11] While broadband SPRs with typically a low Q-factor are beneficial to some applications,[15] such as solar energy conversion, field amplification, photodetection, infrared imaging, bolometry, and manipulation of mechanical resonances, several other applications, such as spectrally selective thermal emission,[16] absorption filtering,[17] SERS,[18] nanolasing,[19] nanolensing,[20] quantum optics,[2a] and optical tweezers[21] need narrow spectral linewidths with high-Q resonances. For example, a narrow resonance peak is lucrative

B. Wang, Dr. P. Yu, W. Wang, Prof. H. Kuo, Prof. H. Xu, Prof. Z. M. Wang
Institute of Fundamental and Frontier Sciences
University of Electronic Science and Technology of China
Chengdu 610054, China
E-mail: peng.yu@uestc.edu.cn; zhmwang@uestc.edu.cn
Dr. X. Zhang
School of Physical Science and Technology
Northwestern Polytechnical University
Xi'an, Shaanxi 710129, China
Prof. H. Kuo
Institute of Electro-Optical Engineering
National Chiao Tung University
Hsinchu 30010, Taiwan
Prof. H. Xu
School of Physics and Technology
Center for Nanoscience and Nanotechnology
and Key Laboratory of Artificial Micro- and Nanostructures of
Ministry of Education
Wuhan University
Wuhan 430072, China
The ORCID identification number(s) for the author(s) of this article can be found under https://doi.org/10.1002/adom.202001520.

DOI: 10.1002/adom.202001520

for the plasmonic sensor as they exhibit giant shifts when detecting trace analytes; the ratio Q/V_{eff}, where Q and V_{eff} refer to the mode Q-factor and effective volume, is used to quantify the coupling strength between a cavity, and thus a Q-factor is important for achieving strong coupling; the plasmonic waveguides take advantage of the light confinement ability, but they suffer from significant propagation loss. It should be noted that photonic crystals and dielectric microcavities have the superiority of obtaining high Q-factors.[22] However, they are not able to support a resonant mode with a subwavelength mode volume in contrast to plasmonic cavities.[23] If one can achieve SPRs with high Q-factors, they would get a strong boost for these devices. However, the resonance width of LSPs usually does not exceed ≈100 nm, and the width of PSPs is typically ≈50 nm due to loss contributions from interband and intraband transitions, leading to a low Q-factor.[24]

Many strategies have been proposed to mitigate or prevent losses in plasmonics, such as searching for better plasmonic materials,[25] hybrid photonic–plasmonic integration,[14] reduction of surface roughness in fabrications,[26] using media with optical gain,[27] and utilizing some unconventional plasmonic resonances.[9,11,28] According to reasonable designs, unconventional plasmonic resonances can be achieved with high Q-factors. Surface lattice resonances (SLRs), which can be attained by arranging the nanoparticles into periodic arrays, is the diffractive coupling of LSPs via in-plane diffraction orders.[29] SLRs can suppress the radiative damping of plasmonic resonance to obtain a high-Q factor, promising for plasmonic band-edge lasing, Bose–Einstein condensation, strong light-matter coupling, etc.[11] Plasmonic Fano resonances and plasmon-induced transparency (PIT) can be observed by breaking the nanostructure's symmetry, reducing or even completely inhibiting the radiation loss, which has useful applications in sensors, optical switches, and slow-light devices.[28a] Moreover, multipolar resonances, plasmonic guided-mode resonances (GMRs), and Tamm plasmon resonances can also be used to decrease the resonance linewidth inunconventional plasmonic resonances.[9,28b,c]

This review article aims to describe some methods for achieving high Q-factor plasmonic resonances and their usages at various application levels. This paper is organized as follows. In Section 2, we introduce design principles for achieving high-Q plasmonic resonances. In Section 3, we focus on describing the physical interpretations and resonances mechanisms of these unconventional high Q-factor plasmonic resonances, including SLRs, multipolar plasmonic resonances, plasmonic Fano resonances, plasmon-induced transparency, GMRs, and Tamm plasmon resonances. In Section 4, we review applications of high-Q plasmonic resonances, such as spectrally selective thermal emission, sensing, single-photon emission, filtering, and band-edge lasing. Finally, we conclude this review with comments and outlook.

2. Design Principles for High-Q Plasmonic Resonances

2.1. Limiting Factors for the Resonance Quality

Q-factor can be characterized by the surface-plasmon dephasing times (T_2), in which the coherently oscillating electrons lose their phase, and they crucially influence the linewidth Γ of the SPR.[30] The relationship between T_2 and Γ can be represented by equation $\Gamma = 2\hbar/T_2$.[31] Typical electron dephasing times in silver are 10–60 fs, and for gold are 1–10 fs in the plasmonic region.[32] Radiation damping and electron–electron scattering are fast decayed in metal nanoparticles, which leads to a short lifetime of SPR, resulting in a broad linewidth of LSP resonance of the particles. Considering different applications that have different definitions of the Q-factor,[31,33] we use commonly-used definition—it can be expressed as $Q = \lambda_{max}/\Delta\lambda = \omega/\Delta\omega$, where λ_{max} is the maximum resonance wavelength, and $\Delta\lambda$ is the FWHM at resonance wavelength.

To improve the Q-factor of the SPRs, we need to understand the factors that influence the linewidth of SPR. For PSPs and LSPs, the linewidth of plasmon resonances is mainly determined by both nonradiative and radiative damping.[18] In the particle plasmon, nonradiative damping occurs via excitation of electron–hole pairs, which can be divided into two categories: intraband excitations within the conduction and interband excitations originating from transitions between d-bands and the conduction band in noble metals, as shown in **Figure 1**a.[31] Suppression of interband damping can reduce the plasmon dephasing rate and increase the Q-factor. This intrinsic nonradiative damping is interrelated with the imaginary part of the dielectric function, which indicates that the energy and the momentum of the collective electrons can be dissipated inside the metal.[34]

For nanoparticles embedded in the matrix, chemical interface effects cannot be neglected because the scattering rate of the conduction electrons is increased.[35] Such chemical interface damping provides an extra nonradiative decay channel for the plasmon resonance. On the other hand, the radiative damping occurs via transforming particle plasmons into photons, which is a process that does not exist in classical physics and needs to be treated with quantum mechanics.[32] Generally,

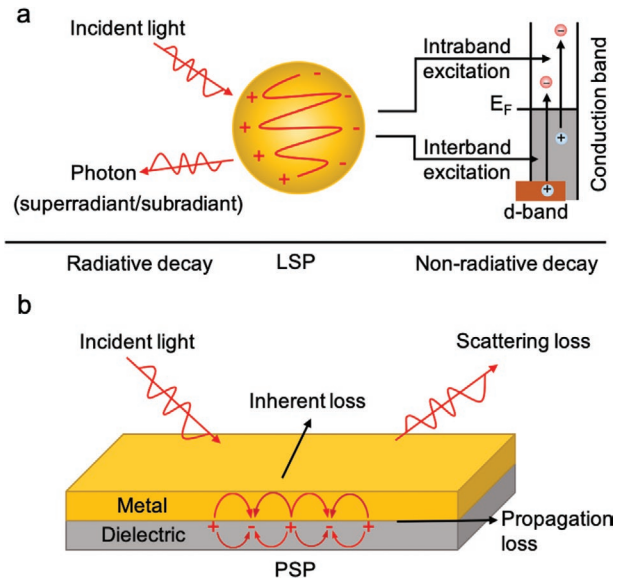

Figure 1. a) Schematic representation of radiative and nonradiative decay of particle plasmons. b) The main process of damping loss in PSPs.

radiative decay can be addressed by coherent couplings between the relevant optical excitations, leading to the super-radiant (bright mode) and subradiant (dark mode) behavior.[24,34] These decays have size-dependent effects.[36] For the size of nanoparticles less than 20 nm, electron-surface scattering is an important dephasing mechanism for the plasmon electrons.[37] As the particle size increases, the contribution of subradiant damping becomes more severe.[18] Moreover, direct emission of electrons, increased Landau damping, and grain boundary scattering can also influence the decay of the particle plasmon.[38]

Especially for the PSPs, the main damping loss can be divided into three parts: scattering loss, propagation loss, and inherent loss, as shown in Figure 1b.[39] Aside from the intrinsic properties of the materials, fabrication limitations such as grain boundaries, surface roughness,[40] and adhesion layers also cause the contribution to plasmon damping.[41] Due to the strong damping effect, the resonance linewidth is several hundred nanometers in the visible and near-infrared, which leads to a very low Q-factor.[42] Thus, the main method to increase the Q-factor is to suppress nonradiative and radiative damping.

Typically, the dampening in LSPs is larger than that of PSPs, leading to a broader spectral linewidth and lower Q-factor in LSPs.[43] For example, the typical linewidth of LSPs is more than 80 nm for Au nanoparticles, but it is ≈50 nm for Au films.[11] Changing the spherical particles into nanorods can also lead to a narrower linewidth.[44] However, changing the size and shape of nanoparticles does not lead to significant improvement of Q-factors, as already intensively proven.[45] For simple nanostructures, the Q-factor is determined only by the complex dielectric constant of the metal, independent of the nanoparticle shape or the dielectric environment, indicating that once the material and resonant frequency are chosen, there is little to do to improve the sharpness of the plasmon resonances.[33]

2.2. Solutions for Achieving High-Q Plasmonic Resonances

Many schemes for achieving high-Q plasmonic resonances have been proposed, as shown in **Figure 2**. Alternative plasmonic materials, such as alloys, heavily doped semiconductors, Dirac semimetals, and graphene, have been investigated, as shown in Figure 2a.[25] These alternative materials have potential applications at different frequencies. For example, graphene has a higher-Q factor in the THz region, and oxide semiconductors are usually lossless at the telecommunication wavelength. The interaction between nanoparticles and the substrate can modify the optical response of the nanoparticle, as illustrated in Figure 2b. Halas et al. used a substrate-induced modification to reduce linewidth and enhance the scattering intensity of the plasmonic nanoparticles.[46] The narrowing spectrum originated from a substrate-mediated hybridization of the dipolar and quadrupolar plasmons, lowering the radiative loss of nanoparticles.[47] Lowering operating temperatures can significantly reduce the collision frequency of electrons, leading to an improved Q-factor, as depicted in Figure 2c.[48] Kim et al. have predicted that Q-factor can be a hundred-fold increased by lowing temperature from 300 to 20 K.[48a] Using proper fabrication techniques, one can reduce the surface roughness of plasmonic nanostructures to boost the Q-factor via reduces the surface collision damping of PSP modes, as shown in Figure 2d.[26] For example, since lithographically—defined nanostructures have more plasmon damping than wet-chemically synthesized nanoparticles, Bosman et al.[26] and Tobing et al.[49] have demonstrated that by encapsulated annealing or decreasing the deposition rate to reduce the grain boundaries, the Q-factor can be further enhanced. Hybrid metal-dielectric nanostructures take advantage of both plasmonic and all-dielectric nanoantennas to compensate for the low Q-factor of plasmonics, as illustrated in Figure 2e.[50] This hybridized

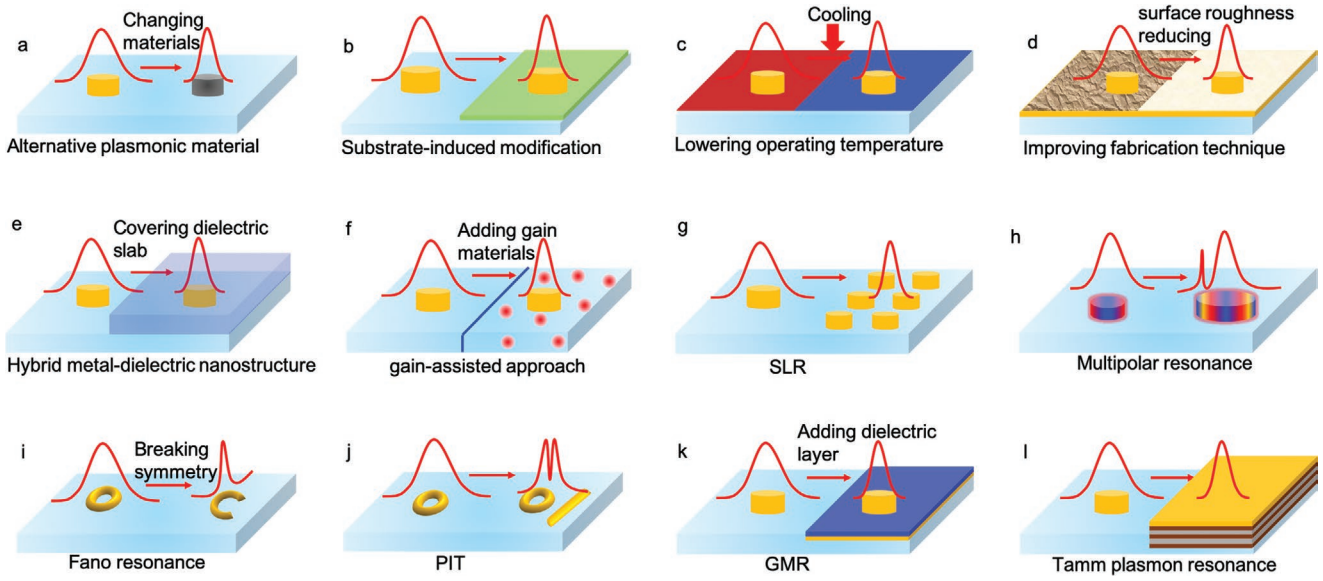

Figure 2. A summary of methods for achieving high-Q plasmonic resonances. a) Alternative plasmonic material. b) Substrate-induced modification. c) Lowing operating temperature. d) Improving the fabrication technique. e) Hybrid metal–dielectric nanostructure. f) Gain-assisted approach. g) SLR. h) Multipolar resonance. i) Fano resonance. j) PIT. k) GMR. l) Tamm plasmon resonance.

plasmonic system can tailor the optical responses and exhibit extremely narrow transmission peaks. An alternative method is to use gain materials or gain-assisted structures to compensate for the intrinsic Ohmic losses in metals, as shown in Figure 2f.[39] By incorporating gain-assisted approaches into plasmonic systems, propagation length of surface plasmon (SPs) and total electric and magnetic field response are enhanced, offering a promise for designing compact devices and surface plasmonic lasers.[51]

By reasonable design, some unique plasmonic resonances can be achieved with high-Q factors. Plasmonic SLRs are mixed light-matter states in periodically arranged metallic arrays when their spacing can support a standing wave of optical-frequency light.[52] The plasmonic SLRs can mitigate losses and reduced the FWHM of the resonances below 10 nm, as shown in Figure 2g. Compared with dipole resonance, higher-order modes can serve as electromagnetic modes that have a lower radiative loss, as illustrated in Figure 2h.[28b] By introducing symmetry breaking, Fano resonances can be achieved, as depicted in Figure 2i. Radiative loss is highly suppressed in the Fano resonances because it does not interact directly with the propagating electromagnetic wave.[53] PIT can be viewed as a special of Fano resonance, while it has a symmetric Lorentzian lineshape, as shown in Figure 2j.[54] Plasmonic GMR is a phenomenon related to subwavelength diffraction grating couple with dielectric waveguides. Due to the presence of the dielectric layer in the guided mode, it has a considerable propagation distance of the light wave, and a high resonance quality is easy to obtain, as illustrated in Figure 2k.[55] With alternating dielectric bilayers (low and high refractive index), Tamm plasmon resonances demonstrate intense and narrow resonances due to low dissipation losses of dielectric layers, as shown in Figure 2l.[56] In Section 3, we will introduce six plasmonic resonance modes toward high-Q resonance.

3. High-Q Factors with Various Resonance Modes

3.1. Surface Lattice Resonances

When arranging nanostructures in 1D or 2D periodic arrays by reasonable design, the interaction among them can strongly be enhanced via near-field coupling and far-field coupling, resulting in an array-induced resonance called SLRs. The SLRs are also called collective resonances and can suppress the radiative damping of plasmonic resonance. SLRs originate from the LSPs coupling with diffractive orders of the array.[57]

Properties and applications of SLRs are comprehensively reviewed in refs. [11] and [58]. Schatz and co-workers first carried out theoretical studies of the SLRs.[59] Using the coupled dipole approximation (CDA) method, they reported that collective excitations in 1D and 2D plasmonic arrays have a possibility of achieving extinction linewidth orders of magnitude narrower than those of an isolated nanoparticle.[52] In 2008, experimental verification of the effect was realized by studying 2D rectangular Au nanoparticle arrays.[60] In the CDA method, an array of nanoparticles is replaced by an array of electric dipoles. The width of SLRs is governed by $\mathrm{Im}(1/\alpha_s\text{-}S)$, where α_s is the polarizability and S is the dipole sum, and it can be compensated by matching $\mathrm{Im}(1/\alpha_s)$ and $\mathrm{Im}(S)$.[11] Although the CDA gives a physical understanding and analytic framework for SLRs, it is not able to describe contribution from higher-order resonances. Multipole methods, such as Doyle's approximation, modified long-wavelength approximation, frequency-domain T-matrix method, boundary element method, and finite difference time domain (FDTD) method, can be used for describing contributions of higher-order in SLRs.[52]

The SLRs can be observed in nanoparticle pairs,[24] 1D chain,[59b] 2D arrays,[29] and 3D structures.[61] The quality and the linewidth of SLRs generally depend on the array period, arrangement, array size, particle size, position or size disorder, and the surrounding medium, as shown in **Figure 3**. For example, the linewidth becomes sharp and pronounced by increasing the period, as shown in Figure 3a.[62] Humphrey et al. demonstrated that no particular array arrangement has an obvious advantage over other geometries in terms of SLR linewidth, as shown in Figure 3b.[63] Using the CDA method, Rodriguez et al. reported that the Q-factor of SLRs could be increased with increasing array size,[64] as shown in Figure 3c. Le-Van et al. experimentally demonstrated that Q-factor could be tuned by changing the nanoparticle size, as illustrated in Figure 3d.[65] By increasing the width of the nanorods from 30 to 56 nm, the Q-factors of the SLRs can increase from 98 to 325. This change can be attributed to the modification in coupling strength between the Rayleigh anomalies (RAs) and LSPs. Concerning disorder, including positional disorder, size disorder, and quasirandom disorder, which affects SLRs. As shown in Figure 3e,f, positional disorder impairs, and particle size disorder broadens the linewidth of SLRs.[66] 2D arrays of gold and silver nanoparticles have been extensively studied but failed to obtain sharp spectral features from theory and experiment.[57b,59a] Auguie et al. explained the phenomenon—previous studies did not take medium environment, incident angle, particle volume, and aspect ratio into account.[29] A homogenous environment is necessary for the SLRs excited at normal incidence. The presence of a substrate can suppress diffractions, while when embedding the arrays into a homogeneous environment, the diffractive coupling between light and lattice surface modes emerges, giving rise to a sharp spectral line feature.[67] For example, Chu et al. designed 2D nanoparticle arrays embedded in the water environment to achieve a grating constant and refractive index matching. Li et al. proposed a novel method to get ultrasharp plasmon resonances and relieve the index-matching requirement.[68] The structure used periodic indium tin oxide (ITO) nanorod arrays vertically aligned on a gold film, which can change the dipole resonance to a monopole resonance. These resonances have ultrasharp lineshapes due to plasmonic photonic coupling.

In the cases mentioned above, SLRs arise from the diffractive coupling of LSPs of individual particles, where the array in the plane confines the dipole moment of the LPRs. Since the scattering energy of in-plane dipole is not strongly localized in the plane of the nanoparticle array, most of the energy is reradiated into the free space without being coupled to adjacent nanoparticles. A new type of subradiant lattice plasmon—an out-of-plane dipolar lattice resonance—has been proposed by Zhou et al.[69] **Figure 4**a shows the designed structure images of Au nanoparticle arrays embedded in a polyurethane (PU)

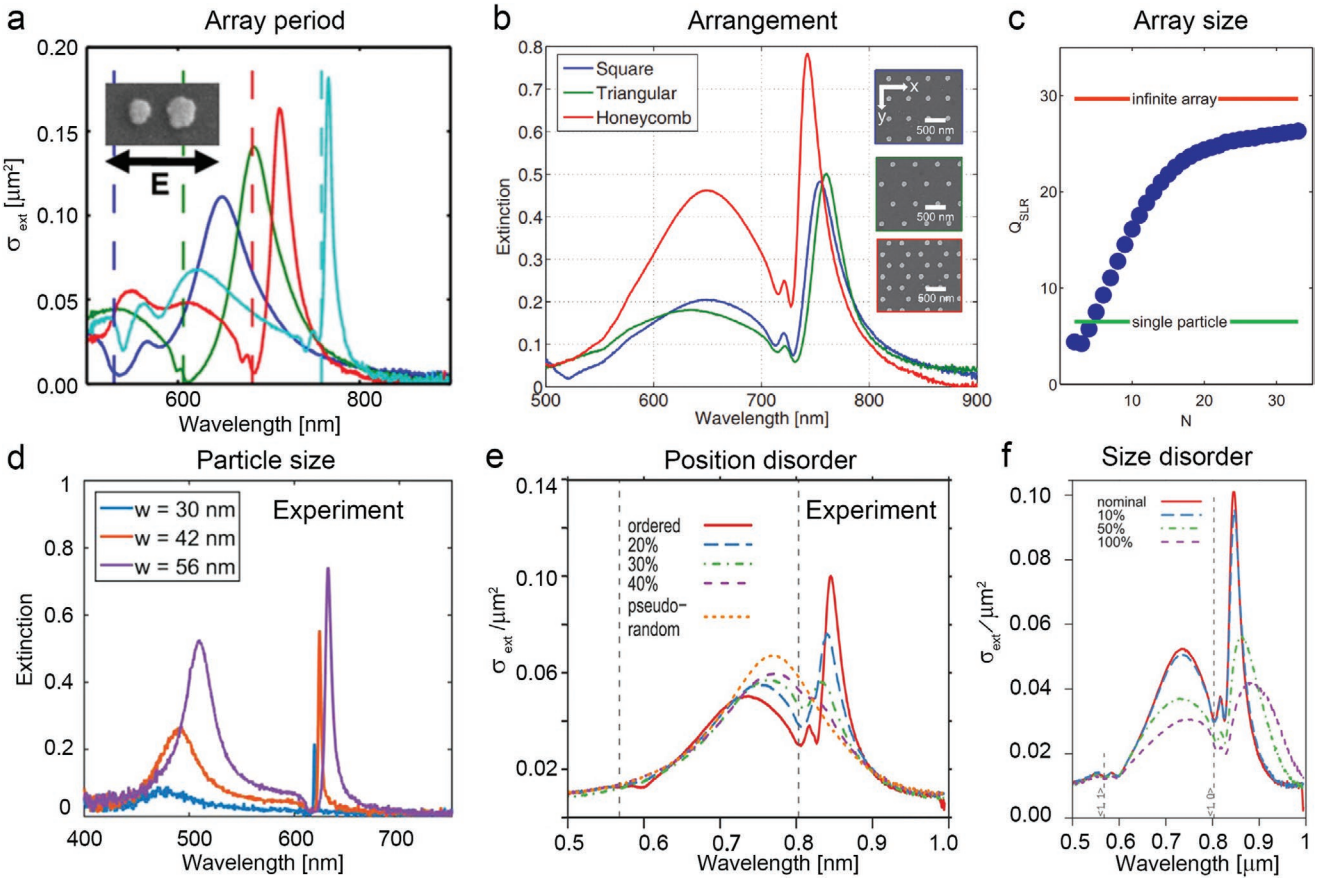

Figure 3. a) Measured extinction cross-section spectra of asymmetric disc dimers (ADDs) arrays with different lattice constants. The structural parameters of two discs are diameter $d_1 = 85$ nm, $d_2 = 115$ nm, height $h = 30$ nm, and a center-to-center separation $c = 150$ nm. The four solid lines, from left to right, represent the lattice constants of ADDs with 350, 400, 450, 500 nm, respectively. b) Measured extinction spectra of particle arrays with different particle arrangement. The insets are scanning electron microscopes (SEMs) of the arrangements; from top to bottom, each represents a square lattice, a triangular lattice, and a honeycomb lattice. c) Calculated Q-factor of SLRs as a function of the number of particles along each dimension of the array. d) Measured extinction spectra of the Ag nanorods arrays at normal incidence. Three nanorods arrays have the same periodicity ($p_x = 340$ nm, $p_y = 420$ nm), but different widths of $w = 30$ nm (blue), $w = 42$ nm (red), and $w = 56$ nm, respectively. e) Measured extinction spectra obtained from five different arrays of nanoparticles. The arrays differed only in the degree of disorder of the particle positions. The nominal particle sizes were $120 \times 80 \times 35$ nm^3. f) Measured extinction spectra from arrays of nanoparticles with regular positions but a variation in particle sizes. a) Reproduced with permission.[62] Copyright 2016, American Chemical Society. b) Reproduced with permission.[63] Copyright 2014, American Physical Society. c) Reproduced with permission.[64] Copyright 2012, Elsevier B.V. d) Reproduced with permission.[65] Copyright 2019, Wiley-VCH. e,f) Reproduced with permission.[66] Copyright 2009, Optical Society of America.

matrix. By changing the nanoparticle height (>100 nm) or incident excitation angle, out-of-plane lattice resonance can be statically tuned, and a narrow resonant linewidth of ≈5 nm can be obtained, as shown in Figure 4b. In this type of resonance, plasmon oscillations are perpendicular to the array plane, and an out-of-plane dipole oscillation can present together with an in-plane dipole oscillation, leading to a narrow subradiant dip. This out-of-plane lattice can strongly trap the incident light and induce a large field enhancement in the nanoparticle arrays. It was shown that SLRs have much worse performances in a less symmetric environment. Based on the advantage of out-of-plane lattice resonance, Yang et al. proposed a metal–insulator–metal (MIM) structure that supported SLRs nanopillar arrays, in which a Q-factor of 147 was obtained in an asymmetric dielectric environment.[61] Recently, an ultranarrow 0.9 nm linewidth in the visible region has been reported using the out-of-plane SLRs method.[70] This out-of-plane lattice plasmons can be used to lower the gain thresholds for surface plasmon amplification by stimulated emission of radiation (spaser).[57a]

Since SPs can interact with each other over long distances, multiscale patterning of plasmonic structures has been presented for novel optical properties.[71] These hierarchical plasmonic structures can significantly narrow resonance linewidth by coupling of single-patch lattice resonance with Bragg diffractive orders. The narrower lattice plasmon resonances are named superlattice plasmon resonances, and a typical structure is shown in Figure 4c.[72] Compared with infinite nanoparticle arrays, the 2D hierarchical arrays show a narrower superlattice plasmon resonance, in which a 7 nm FWHM is illustrated in Figure 4d. The superlattice structure can support multiple band-edge modes and manipulate the output behavior of different lasing modes.[19b]

Another way to narrow lattice resonance linewidth is to use the plasmon hybridization methods by designing a hybrid

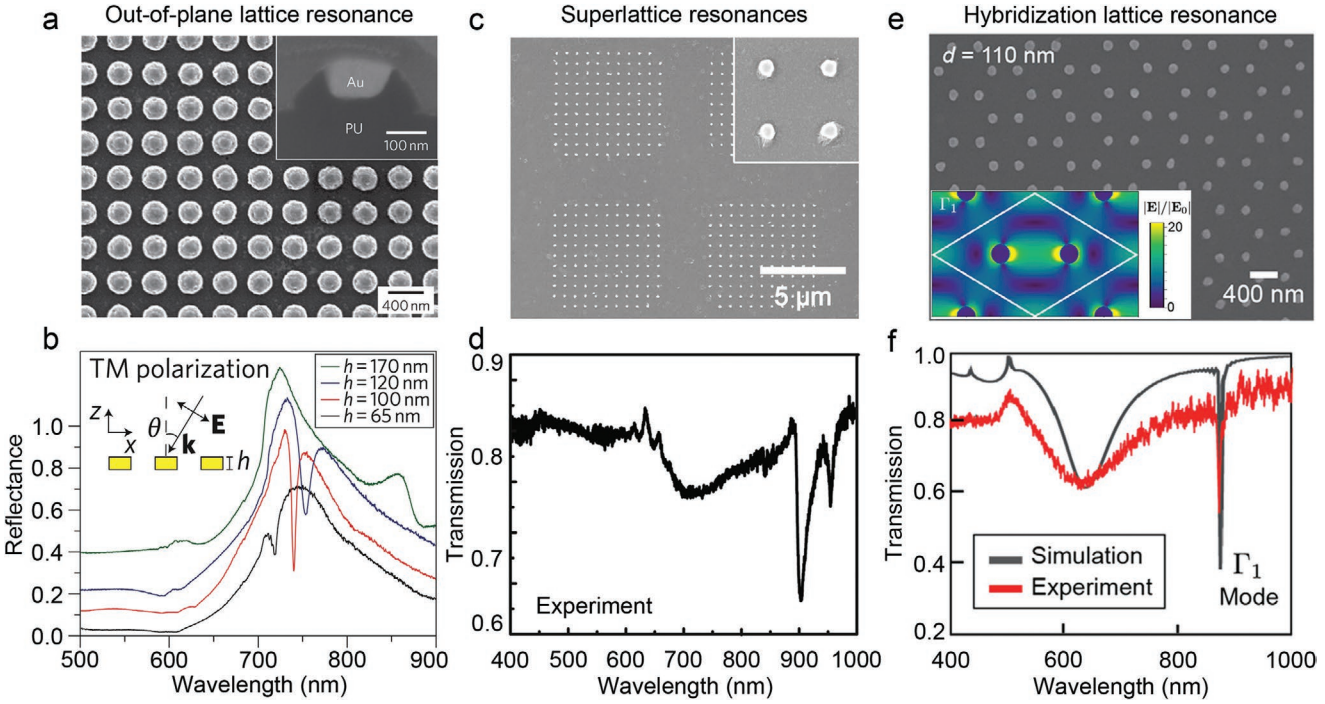

Figure 4. a) SEM images of the out-of-plane lattice structure, where Au nanoparticle arrays are embedded in the PU matrix. The diameter of the Au nanoparticle is 160 nm, the period is 400 nm. b) Measured height-dependent reflectance spectra of Au 2D nanoparticle arrays under TM-polarized light. The height of Au particle h = 65, 100, 120, 170 nm. The narrow spectral peak strongly depended on the height. c) SEM images of 2D superlattice nanoparticle arrays and d) measured transmission spectra. The nanoparticle diameter is 140 nm, and the period is 600 nm. The patch side length is 6 μm, the period is 9 μm. e) SEM image of a fabricated honeycomb lattice of Ag nanoparticles. (Inset) Calculated electric field distributions at Γ_1 mode, which shows the asymmetric spatial distributions. f) Calculated and measured transmission spectra of the lattice. The diameter of the Ag nanoparticle is 110 nm, height is 50 nm, and the lattice period is 400 nm. a,b) Reproduced with permission.[69] Copyright 2011, Springer Nature. c,d) Reproduced with permission.[72] Copyright 2015, American Chemical Society. e,f) Reproduced with permission.[73b] Copyright 2019, American Chemical Society.

structure or higher multipole resonance coupling.[73] If SLRs are excited in this hybrid structure, strong interactions of the near field in SPs can be observed, and the optical response is completely modified accordingly.[74] Based on this method, Baur et al. proposed a periodic array with a multiparticle unit cell structure to control the optical response of narrow bandwidth.[73a] The system supports the collective plasmon resonance, which is quite different from that SLR supported by a single nanoparticle. The interaction between single lattice resonances can be canceled or maximized by controlling the particle position. Moreover, non-Bravais lattices structure have been reported to obtain the hybridization lattice resonance.[73b] Figure 4e shows the structure that can produce SLR hybridization because of the different orders of LSPs coupling in the adjacent nanoparticles. Lasing action proves that dipole-quadrupolar coupling is allowed at the Γ point where asymmetric electric field distributions show multipolar LSP superposition. Figure 4f is the measured transmission spectrum of the lattice structure showing a sharp resonance with an FWHM of 5 nm, as shown in Figure 4f. Thus, hybrid SLRs provide another route for achieving high-Q resonance.

Other methods have been used to obtain high-Q lattice resonance. Li et al. demonstrated that periodic all-metal nanowire and nanoring arrays could be used to realize ultranarrow linewidth.[75] When SLRs were excited, two narrow absorption peaks with 9 and 12 nm FWHM were achieved, respectively. In addition, quadrupolar lattice resonances have been excited by cylindrical vector beams, which exhibits a narrow line shape with an FWHM of ≈30 nm.[76] Noble metal plasmonic materials can be substituted by other materials with low interband loss properties to mitigate material losses.[25,77] Doped graphene has been used to excite SLRs, leading to a strong optical field enhancement.[78] Yang et al. used Al nanoparticle arrays embedded in polydimethylsiloxane (PDMS)—the spectra can be dynamically modulated, exhibiting high-Q resonances with FWHM of 5 nm. This offers a route to realizing tunable spectra for practical application.[79] For high-temperature applications, SLRs using refractory titanium nitride (TiN) 2D structures were achieved in the communication wavelength range, with a Q-factor value of 2000.[80]

In summary, SLRs offer potential prospects to suppress radiative losses due to the diffractive coupling of the LSP associated with individual nanoparticles, achieving remarkably narrow linewidth down to a few nanometers. The typical resonance properties of SLRs are discussed in this section. Compared with an individual plasmonic nanoparticle with a broadband line width (FWHM > 100 nm), a nanoparticle array in a uniform dielectric environment can exhibit ultrasharp SLRs with FWHM < 10 nm. However, the problem of SLRs is that the spectral intensity is usually weak. By coupling SLRs mode with various types of matters, one can achieve enhanced performance in many possible applications, such as quantum optical source, lasing, ultrasensitive biodetection, etc.

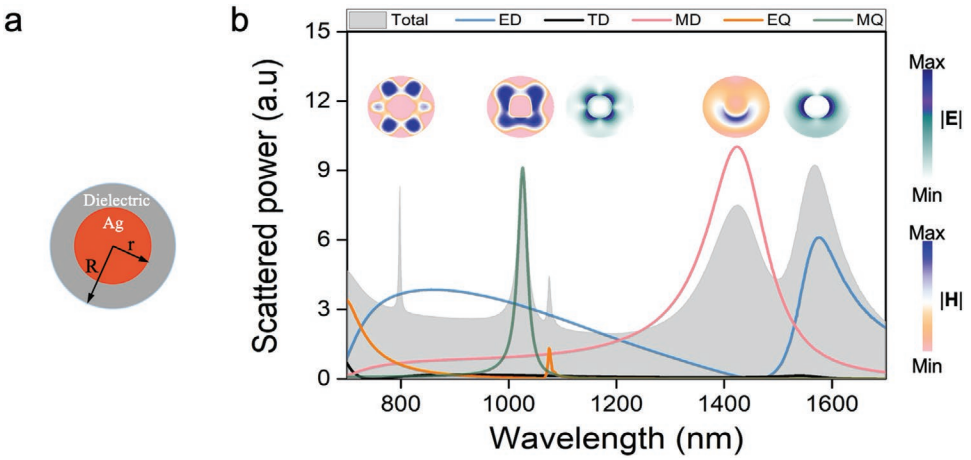

Figure 5. a) Cross-section view of the Ag core–shell structure, where $r = 76$ nm, $R = 200$ nm, and the refractive index of the dielectric is 3.6. b) The scattered power and the field enhancement distribution for the core–shell structure. The gray background represents the total scattered power. The peaks from right to left are generated by electric dipoles, magnetic dipoles, electric quadrupoles, magnetic quadrupoles, and magnetic octupoles, respectively.

3.2. Multipolar Resonances

When the particle size is much smaller than the incident wavelength, the electric field drives the conduction electrons to oscillate to form a dipole resonance mode. In contrast, when the particle size is comparable to or larger than the incident wavelength, the dipole mode is redshifted, forming a broad resonance, accompanied by multipole modes generated at high frequencies.[81] The multipole mode is subradiant (dark mode), and it has weak radiative damping when compared with that of the dipole. Therefore, single multipolar resonance can be utilized to obtain a high-Q factor due to the reduced radiation damping and weaker coupling with light.[82] To compare dipole and multipolar resonances, we theoretically calculated scattering cross-sections of a metal-dielectric core–shell nanoparticle using the Cartesian multipole decomposition method[83] to get the single multipolar scattered power, as shown in **Figure 5**. In essence, high-order electric and magnetic resonance have an obvious higher Q-factor than that of the first-order dipole resonance.

For a symmetric structure, dark plasmon modes cannot be directly excited by a plane wave. Alternatively, it can be stimulated by nonoptical means such as electron beams impinging in the near-field region.[84] For example, electron-energy-loss spectroscopy (EELS) can be used to excite the single nondipole mode[84] or multiple modes.[85] Focused radially-polarized beams show opportunities for exciting the higher-order LSP resonances and enhancing the extinction efficiency.[86] Also, dipole emitters can be used to excited dark surface-plasmon modes as they do not radiate or couple incident plane waves, and thus they do not have any radiative losses.[87] Multipolar resonance can be excited by the incident electric field directly via breaking the excitation symmetry.[88] Moreover, owing to the dark mode of higher-order resonance, resonant spectra of multipole have a different angle- and polarization-dependent properties compared with their dipole counterparts.[89]

Various multipolar plasmonic resonances can be excited by controlling particle size,[90] shapes,[91] symmetry breaking,[92] as well as in large planar metamaterial structures.[93] For instance, individual sliver nanorice[94] or nanorod[95] can also be used to generate multipolar resonances by oblique illumination, and their multipolar plasmon resonances linewidth can be observed from the theoretical calculation. **Figure 6**a shows the experimental observation spectra of multiorders resonance in a single Ag nanorod at different lengths.[95] With the length of nanorod increases, high order modes can be observed, and the resonance peak position is also changed. Figure 6b shows the measured Q-factors with several multipolar peaks on an Al nanorod, and it reveals that high-order resonance can improve the Q-factor.[96] Besides, nanoparticle dimers can be predicted not only to generate the multipolar resonance (Figure 6c) but also to give rise to collective multipolar oscillations.[97] Other methods, such as using an elliptical split nanoring to suppress the radiative damping and generate a high-order resonance, have been put forward to excite multipolar resonances.[98] For these single nanostructure, the emission intensity is relatively low, as shown in Figure 6d. Giannini et al. demonstrated that SLR modes could couple the multipolar resonance and enhance emission efficiency and Q-factor significantly.[28b] The multipolar resonance mentioned above usually refers to longitudinal plasmons. Tobing et al. have demonstrated that an unexplored hybrid magnetic–electric mode in ultrasmall Al u-shaped and v-shaped split-ring resonators (SRRs) at short visible wavelengths, which terms as transverse plasmons.[99] The preferential excitation of transverse plasmons in multipolar resonance may be another way to obtain high Q-factors.

In summary, single multipole resonance can generate a high-Q resonant factor due to their weak radiative damping theoretically. However, it is hard to obtain experimentally, and the reradiation energy is smaller because these resonances cannot couple efficiently to far-field radiation, leading to a strong reduction in emission efficiency.[28b] Moreover, their resonant frequencies are very close to each other and easy to form a broad spectrum with an overlap. Thus, single multipolar resonance is difficult to be excited and observed. Multipolar resonance can be enhanced by coupling polarized light with antisymmetric distribution due to the electrodynamic retardation between the multipole resonance and the diffraction field in the plane of the array.

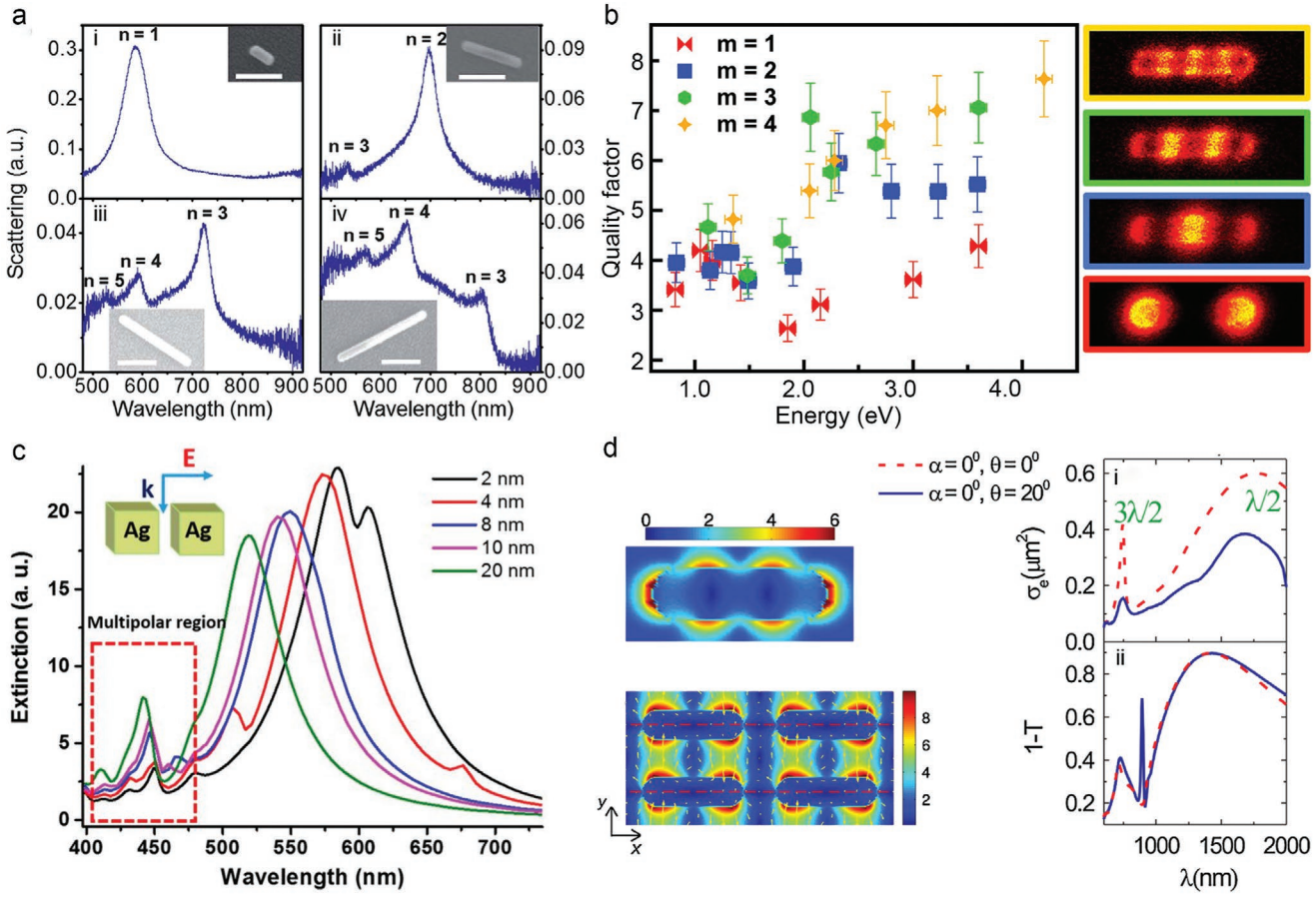

Figure 6. a) Dark-field scattering spectra of Ag nanorods with different lengths. The diameter of Ag nanorods is 35 nm, and their lengths are 104, 258, 426, 497 nm for i, ii, iii, and iv, respectively. The resonant orders are denoted on top of each peak. (Inset) SEM images of the corresponding nanorods and the scale bars are 200 nm. b) Left: Measured Q-factors as a function of their energy of resonances, where $m = 1$ represents dipole, $m = 2$ represents quadrupole and following modes of order up to 4. It shows that the dipolar modes have relatively low Q-factors between 2 and 4. For $m = 4$ modes, the Q values can reach higher from 5 to 8. Right: measured EELS intensity maps of the corresponding plasmonic structure from $m = 1$ to 4 (from bottom to top). c) Calculated extinction spectra for the Ag nanocube dimer at varying separation distances (2, 4, 8, 10, and 20 nm). d) The electric field and the calculated extinction cross-section of single Au (i) and array (ii) of the nanoantenna. For a single Au nanorod, the electric field exhibits a four-lobed (multipolar) distribution at the frequency of the $3\lambda/2$ resonance. The electric field of the array shows that antisymmetric distribution along the long axis (red dashed lines). The gold nanoantenna array shows a narrower and larger extinction spectrum than individual nanoantenna due to the collective multipolar resonance under oblique incidence, which indicates that the intensity of multipolar resonance can be enhanced by SLR modes. The structure of a nanoantenna has a height of ≈38 nm, length of ≈450 nm, and width of ≈130 nm. The lattice constant of the array $a_x = 600$ nm and $a_y = 300$ nm, and the dimension is 3 × 3 mm^2. The nanoantenna array is placed on a glass substrate covered by a layer of PVB with a thickness of 50 nm. The incident electric field is polarized along the x-axis, the wave vector is in the (y, z) plane. a) Reproduced with permission.[95] Copyright 2013, The Royal Society of Chemistry. b) Reproduced with permission.[96] Copyright 2014, American Chemical Society. c) Reproduced with permission.[97] Copyright 2019, National Academy of Sciences. d) Reproduced with permission.[28b] Copyright 2010, The American Physical Society.

3.3. Plasmonic Fano Resonances

Another promising method to suppress radiative damping is to use plasmonic Fano resonance. In complex plasmonic nanostructures, the radiative coupling of dipolar (super-radiation) and multipole (subradiation) resonances give rise to the Fano resonance.[100] Many review articles have discussed the principle and application of the Fano resonance.[28a,101] Fano resonance can be obtained by symmetry breaking, leading to a spectral interference between broad continuum resonance and a narrow discrete resonance, and then form an asymmetric peak-and-dip spectral profile, as illustrated in **Figure 7**a.[102] As the Fano resonance can reduce or even completely inhibit the radiation loss in plasmonic nanostructures, a high Q-factor is easily attainable in the system. Various nanostructures have been designed and explored, such as single,[103] double,[84,104] or multiple[105] symmetry-breaking metallic nanostructures, waveguide-coupled structures,[106] metamaterials, and metasurfaces.[53,107] Controlling the phase of light in symmetric structures, such as use focused cylindrical vector beams,[102b] can also be used to generate Fano resonance.

Here, this review highlights the ultranarrow Fano resonance because it is challenging to realize not only due to radiative losses but also Joule losses. In Section 3.1, we have discussed that SLR can be used to generate the Fano-type lineshape due to the coupling of collective diffractiveand LSPs. For the plasmonic Fano system, a unit cell of the nanostructure can give rise to Fano resonance, which is quite different from SLR. For

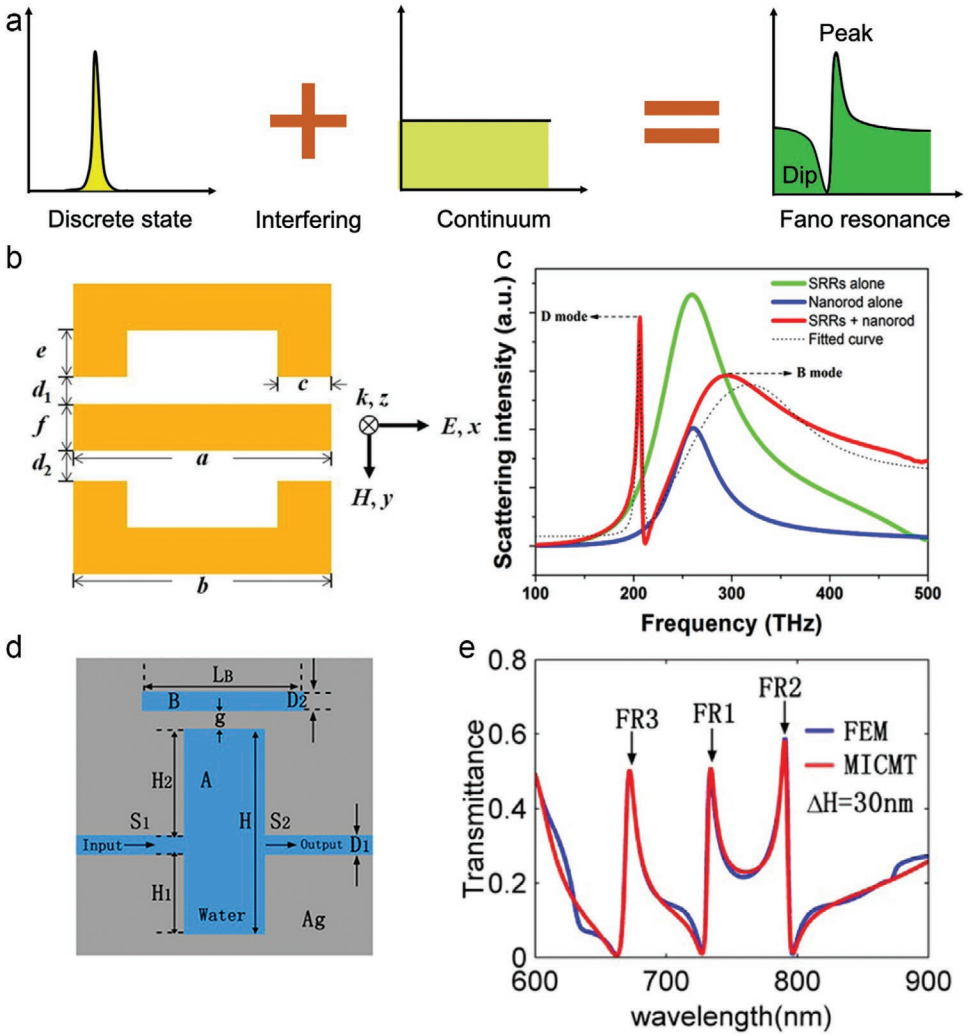

Figure 7. a) Illustration of the Fano resonance as a superposition of the Lorentzian line shape of the discrete level with a flat continuous background and form an asymmetric peak-and-dip spectral profile. b) Schematic diagram of the designed planar plasmonic structure. The corresponding geometric parameters are given as follows: $a = b = 300$ nm, $d_1 = d_2 = 30$ nm, $c = e = f = 60$ nm, and the thickness is 60 nm. c) Simulated scattering spectra of SRRs alone (green), nanorod alone (blue) and, SRRs/Rod (red) structure. d) Schematic diagram of the plasmonic waveguide structure, consisting of two MIM waveguides and two rectangular cavities. e) The finite-element analysis method (FEM) (blue lines) and multimode interference coupled-mode theory (MICMT) (red lines) simulation results of the transmission spectrum of the asymmetric plasmonic system, where $\Delta H = H_2 - H_1$. b,c) Reproduced with permission.[109] Copyright 2013, Optical Society of America. d,e) Reproduced with permission.[112] Copyright 2016, Optical Society of America.

a simple single metallic nanostructure, the symmetry can be easily broken by changing the shape or location of the nanostructure, which provides a convenient way to excite or couple subradiant modes.[108] Based on this strategy, Wang et al. proposed a planar plasmonic structure, as shown in Figure 7b. It is composed of double symmetrical U-shaped SRRs and embedding a metallic nanorod between the two SRRs to excite the resonance mode.[109] In the stacked nanostructure, two Fano resonances were achieved in the near-infrared region due to a strong interplay between a broad bright mode and narrow dark modes, as shown in Figure 7c. Using the dark mode in the Fano resonances, it exhibited a high refractive-index sensing sensitivity of 1360 nm RIU^{-1}. Moreover, another symmetry breaking method can be introduced by using a dielectric substrate with an Ag nanocube.[103] The substrate-induced Fano resonances can be formed by coupling a dark quadrupolar and a bright dipolar plasmon mode at the sharp corners of the cube, which can significantly narrow the width of resonance. In contrast to a single metallic structure, a metamaterial absorber is easy to be integrated, and the absorption band is convenient to be adjusted, which provides a simple method to generate the Fano resonance.[110] For example, Cao et al. proposed an asymmetric split ring planar metamaterial structure. By changing the degree of structural asymmetry to cause destructive interference, the value of the Q-factor could be tuned, and an optimum Q-factor value of 227 was observed at terahertz frequencies.[53] Zhang et al. introduced an asymmetric double elliptical cylinder resonator array on the top layer of the structure of the metamaterial.[111] The array can generate antiphase currents induced by the quadrupolar mode, and a strong magnetic field is confined in the gap, decreasing the radiative loss of the Fano mode. With theoretical calculations, an 8 nm FWHM absorption peak

is observed, with the absorption amplitude exceeding 99% at 930 nm.

Another way is to use the waveguide-coupled structures to arouse the Fano resonance. In these structures, the metallic nanostructure arrays are deposited on a dielectric layer, in which metallic nanostructure arrays can generate a broad radiant mode, and the low loss dielectric waveguide can introduce the narrow subradiant mode.[101] Thus, a much sharp Fano resonance can be easily obtained by coherent interaction with the coupled two modes. In this system, an effective way is to use the cavity structures.[112] Figure 7d exhibits a waveguide-cavity structure, which comprised two MIM waveguides with two rectangular cavities. Triple narrow Fano resonances were observed in the transmission spectra, as shown in Figure 7e. This result indicates that a strong trapped resonance occurs in the cavity resonator, resulting in a narrow transmission peak. Lee et al. utilized capped gold nanoslit arrays on a polymer film to enhance Fano resonance. The structure can also produce a cavity resonance mode and a plasmon resonance mode; a 3.68 nm FWHM was measured at the visible light range.[113]

Other methods have been put forward to generate high-Q Fano resonance. For example, Srivastava et al. proposed a superconductor metasurface structure to lower the radiative loss in Fano resonance.[114] Two overlapping Fano resonances may give rise to the birth of a new sharp asymmetric resonance when they are located very close to each other.[115] Fano resonances in these designed structures exhibited distinct sharpness and field enhancements, and they are typically more sensitive to changes in the refractive index of the environment, which have promising applications for biochemical sensing. The plasmonic Fano resonance also promises applications in lasing, switching, near-field imaging, and slow-light devices. Further studies can be done by integrating Fano resonance structure with electro-optic applications, such as nanotubes, quantum dots (QDs), or conventional semiconductors.

3.4. Plasmon-Induced Transparency

Electromagnetically-induced transparency (EIT) is a quantum phenomenon arising from a three-level atomic system in which two different excitation pathways interference with each other, as shown in **Figure 8**a.[116] In the three-level atomic system, the transition between the metastable state |1> and excited state |2> can be controlled by a pumping laser, while the probe laser drives the transition between the excited state |2> and the ground state |0>. A usual absorption lineshape will be observed without pumping (Figure 8b), but a dip in the absorption spectra can be obtained after introducing the pumping (Figure 8c) because the pump suppresses absorption at the resonance wavelength. The mechanical model can be used to simulate the EIT[117]—it can be described by the mechanical system subjected to a harmonic driving force, as shown in Figure 8d. In this system, first oscillator A can be represented as a bright mode, which is subject to a harmonic force. Besides, the oscillator A can be driven by external force. When the external power is transferred from the harmonic source to A, a usual resonance linewidth can be seen (Figure 8b). The second oscillator B is indicated as the dark mode, which can be excited only through the spring with the constant K and k_2. If we allow B to move, the absorption profile is modified (Figure 8c). Thus, The EIT profile is shown due to the interference between "bright" and "dark" modes. The EIT is promising for a slow light system, sensor, data storage, and low-loss metamaterials.[54] In plasmonic systems, the EIT-like properties are referred to as plasmon-induced transparency (PIT), characterized by the

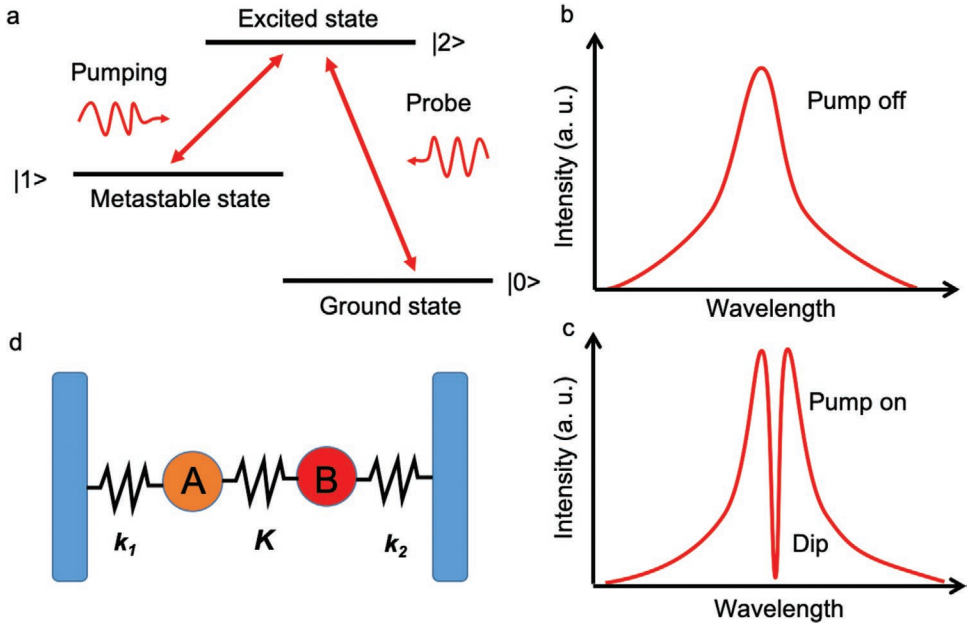

Figure 8. a) A three-level atomic system used to illustrate EIT. b) The observed absorption spectra without pumping. c) The obtained absorption spectra with the pumping. d) A mechanical model is used to simulate EIT. Two oscillators A and B are attached to three springs with spring constants k_1, k_2, and K.

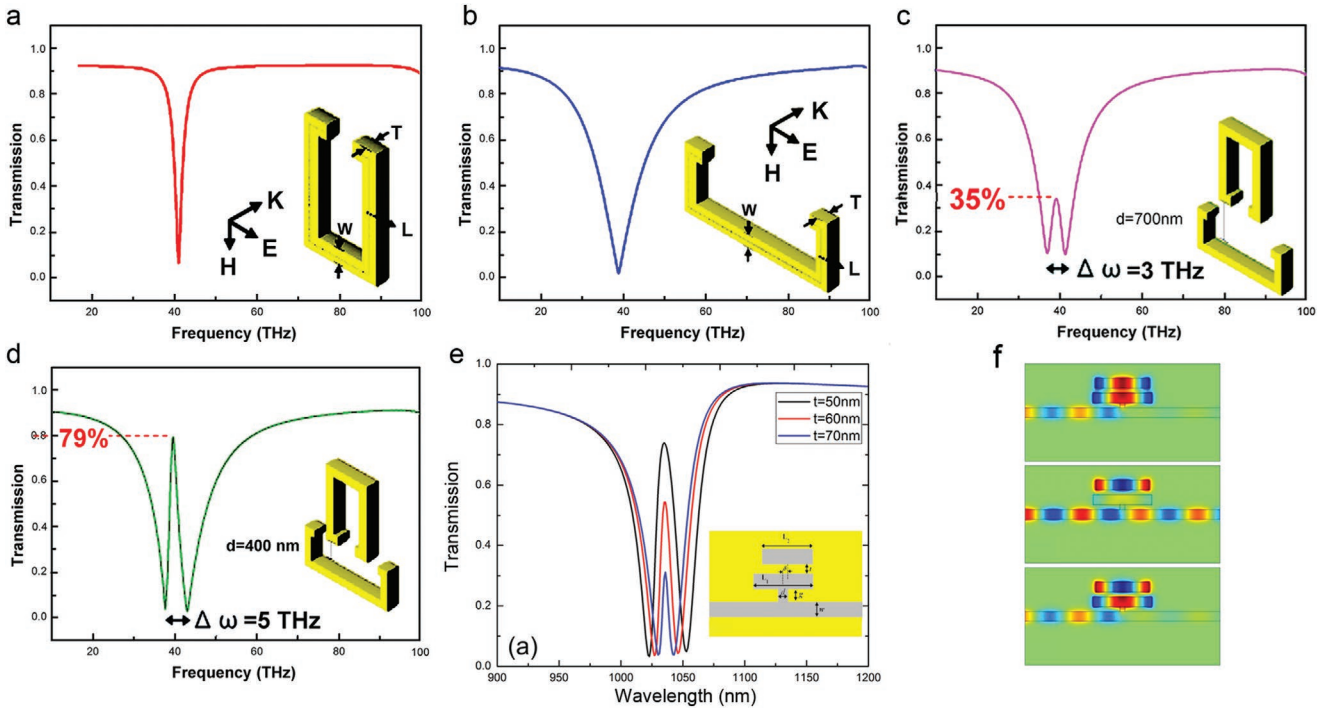

Figure 9. a) The simulated transmission spectrum of the narrow SRR element (SRR_n) and b) the wide SRR element (SRR_w). Insets: illustration of the respective resonator structure. Structural parameters of SRRs: $W = 0.1$ µm, $T = 0.05$ µm, total length $L = 1.88$ µm (in SRR_n), $L = 1.92$ µm (in SRR_w). c) The simulated transmission spectrum of coupled resonators with the spacing of 400 nm and d) 700 nm. Insets: illustration of the coupled resonator, respectively. e) The simulated transmission spectrum of the MIM waveguide structure with the distance t between two resonators of 50, 60, 70 nm. Inset: Schematics of the waveguide structures, in which $L_1 = 600$ nm, $L_2 = 550$ nm, $\delta = 0$, $d = 50$ nm, $g = 50$ nm, $w = 100$ nm. f) Magnetic field distribution at the wavelengths of 1023, 1035, and 1053 nm when t is equal to 50 nm. a–d) Reproduced with permission.[121] Copyright 2009, Optical Society of America. e–g) Reproduced with permission.[132] Copyright 2014, Optical Society of America.

frequencies of a narrow transmission band and a broad absorption band match.[28a] Thus, PIT can also be viewed as a special case of Fano resonance, but it exhibits a symmetric Lorentzian lineshape. Moreover, PIT can enhance the dark mode resonance energy and decrease the bright mode lineshape.[118]

Since Zhang et al.[54] first proposed the concept of PIT, many structures have been widely investigated theoretically and experimentally to get narrow and broadband spectral from the destructive interference in recent years.[119] In 2009, the PIT effect was first experimentally demonstrated using a stacked optical metamaterial,[120] and since then, the phenomenon is realized from various geometric structures in classical metamaterial systems at different frequency regions. Typical structures to realize the PIT effect are shown in **Figure 9**a–d.[121] One resonator is used to generate a narrow sub-radiant mode in Figure 9a, while another resonator is used to obtain a broad super-radiant mode, as shown in Figure 9b. By coupling the two resonance modes, a sharp PIT spectrum appears, and it can be modulated by the spacing of two resonator constituents, as demonstrated in Figure 9c,d. Wang et al. combined a simple nanoring and nanorod compound metamaterial structure by adjusting the geometric parameter of the structure, and a high-Q factor of 97 with a 60% transmittance window was achieved at optical frequencies.[122] Afterward, their team used a stacked metamaterial structure consisting of a solid bar and a slot. By coupling the magnetic response and the electric resonance, a near-complete absorption resonance with an 8 nm linewidth at optical frequencies is achieved.[123] Recently. Vafapour et al. reported a planar nanostructure metamaterial, which consists of three silver bars deposited on a glass substrate. Two vertical bars were used as a bright plasmonic mode, and the horizontal bar was used as a dark plasmonic mode. By adjusting the bright mode and dark mode in the asymmetric structure, the PIT-like effect was excited, which shows a very sharp resonance with the bandwidth of ≈2.96 nm, and the corresponding Q-factor is 411.[124] Besides, by integrating the graphene into metamaterial structure, Q-factor and transmission intensity can be further enhanced due to the decreased Ohmic loss.[125] Multiple PIT spectral responses were observed in multilayer graphene cavities.[126] Furthermore, by changing the spatial configurations of "metamaterial molecules,"[127] or integrating photoactive silicon,[128] thermally active superconductor-metal,[129] and graphene microstructures,[126] the PIT spectral response can be controlled and tuned.

Another way to mediate the coupling is to use the plasmonic waveguide structure. Various plasmonic waveguides have been proposed and demonstrated to show PIT spectral response.[50,130] Zentgraf et al. proposed a hybridized plasmonic waveguide system that consists of a gold nanowires array and two dielectric slabs.[50] As the nanowires were embedded in a waveguide material, the LSPs and the waveguide mode can be coupled by changing the spectral mode position to form a waveguide-plasmon hybridization. By changing the interference between the two excitation pathways, a 0.5 nm FWHM can be

achieved. Since MIM waveguides utilize gap surface plasmons, one can obtain extremely tight mode confinement with moderate propagation loss.[119] Typically, MIM waveguides consist of bus and resonator waveguides, which can be used to generate radiative and subradiant modes.[131] Thus, EIT can be achieved by coupling radiative (coupled to a bus waveguide) and subradiant (not coupled to the waveguide) resonator or canceling the opposite contribution of two detuned resonances.[119,132] By adjusting the resonant waveguide and bus waveguide phase-matching, a high Q-factor PIT effect can be achieved. Wang et al. proposed a three-level energy systems structure to realize and explain the PIT effect; the structure consists of a bus waveguide and two radiative resonators, as shown in Figure 9e (inset).[132] The bus waveguide and two resonators represent the ground state, the metastable state, and the excited state, respectively. The first resonator couples the bus waveguide to excite bright mode, and the second resonator can only be coupled to the bus waveguide through the first resonator, which works as the dark mode. Figure 9e,f shows that by adjusting the relative position between the two resonators, PIT behavior can be well engineered. Moreover, based on the phase-coupled effect, various stub resonators with MIM waveguides can be used to obtain multiple PIT spectral responses, and the bandwidth of FWHM can be decreased to 6 nm, which is much smaller than the single stub resonator.[133] By adopting these multistub resonators, Chen et al. achieved a higher Q-factor of 427.[134] It should be noted that MIM plasmonic waveguides can simultaneously generate Fano resonance and PIT effect, which can be utilized to achieve multispectral switching.[118]

The PIT effect can also be generated by using a photonic nanogap antenna system coupled to a QD or molecules, which is called quantum-dot-induced transparency.[135] Manjavacas et al. presented a structure that consists of a silver spheroid dimer with a QD embedded at its center. By introducing the QD transition linewidth, a transparency dip appeared in both extinction and scattering spectra. In the system, the QD was treated as a single dipole, which can form a competitive absorption relationship with metal nanoparticles. Due to the Ohmic loss and weak controllability of metal-based plasmonic in visible and near-infrared regions, the Q-factor and PIT effect is generally hindered.[130,136] Dielectrics are commonly used to decrease radiative loss, and thus increasing the proportion of the dielectric layer in PIT systems may be another way to obtain a high Q-factor resonance.

3.5. Guided-Mode Resonances

The SP is a surface wave supported by metal-dielectric interfaces, which can be tightly confined at the interface so that the light can be confined and guided beyond the diffraction limit, allowing for extreme nanofocusing.[137] Because of these unique properties, various types of plasmonic guided-mode structures have been proposed and investigated to guide SPRs for potential nanophotonic devices, such as MIM/IMI multilayered structures,[138] metal strips,[139] wedge,[140] nanowires,[141] tapered grooves,[142] nanoparticles chains,[143] and hybrid plasmonic waveguides.[55] These waveguide structures can confine electromagnetic energy strongly near the metal-dielectric interface.[144] However, Ohmic losses and/or radiation (e.g., scattering) limit the propagation distance of SP in these waveguide structures. For example, single metal strips have a high dissipative loss because of their rough surfaces.[144] Many waveguide designs have been investigated to overcome this limitation and to increase the Q-factor. In this section, we discuss the plasmonic GMRs, such as Fabry–Pérot (FP) resonance and cavity mode (alternatively called gap plasmon resonance).

FP-like resonance has been widely discussed in plasmonic nanostructures.[145] In these structures, horizontal and vertical placed films are acting as high-quality optical mirrors. This FP-like structure can concentrate SPs, and thus radiative damping of the metal can be sharply decreased.[145–146] Therefore, by choosing appropriate structure parameters and material properties, the powers of the internal field and bandwidths of resonance spectra can be tuned. For example, Zhu et al. designed a metallic trench SP–FP resonator,[147] as shown in **Figure 10**a,b. When the white-light illuminates the cavity, SPs can be launched. These SPs can propagate across the cavity and be reflected from the sidewalls. In this case, a slit under the cavity floor with subwavelength width is used, as shown in Figure 10b. This slit allows probing of the transmission mode close to their maximum intensity. Figure 10c shows that the resonator exhibits a high-Q factor of 310 at the visible-frequency. MIM/IMI multilayered structures are widely used in plasmonic GMRs.[138] Figure 10d–f shows a typical MIM FP microcavity structure.[148] The structure consists of two asymmetric FP cavities, both with the gold as a back reflector. Light can be tuned by changing the cavities length of L_1, and a 15 nm FWHM bandwidth can be obtained at $\lambda = 857$ nm, as shown in Figure 10g. In this FP cavity, LSP mode and standing wave can be strongly coupled with constructive interference, and the resonance thereby is enhanced. Similar structures have also been explored to narrow the linewidth. By changing the nanoslit microcavity structure to a metal-MIM structure, a nearly perfect absorption with a narrow FWHM of 1.11 nm was realized in the infrared region.[149] Subsequently, Wu et al. put forward a structure by adding a triangular nanoribbon between the gold nanoribbons, and an absorption bandwidth of 1.82 nm in the visible region was achieved.[150] Fix et al. demonstrated that two plasmonic FP cavities could be coupled and give rise to interference-effect.[151] The Q-factor can be tuned by changing the cavity width. Also, Thijssen et al. put forward a nanomechanical geometry MIM waveguide. It can couple mechanical oscillators to plasmonic mode, experimentally achieving a high Q-factor of 634 in the optical region.[152]

Another way to increase the Q-factor is to use a hybrid plasmonic waveguide.[55] For example, the hybrid plasmonic waveguide can couple SPs waveguide with a dielectric waveguide, which can decrease plasmon propagation loss and increase propagation distance.[153] Such hybrid plasmonic waveguides can also couple to FP resonances with cavity mode and reduce the total loss.[154] Sarkar et al. proposed a hybrid plasmonic waveguide to decrease the radiative loss via colloidal plasmonic self-assembled grating, as shown in Figure 10h.[155] They used a plasmonic grating fabricated by colloidal self-assembly and an ultrathin injection layer to guide the resonant modes selectively, as illustrated in Figure 10i. The measured transmission spectrum at 902 nm (Figure 10j) shows the presence of

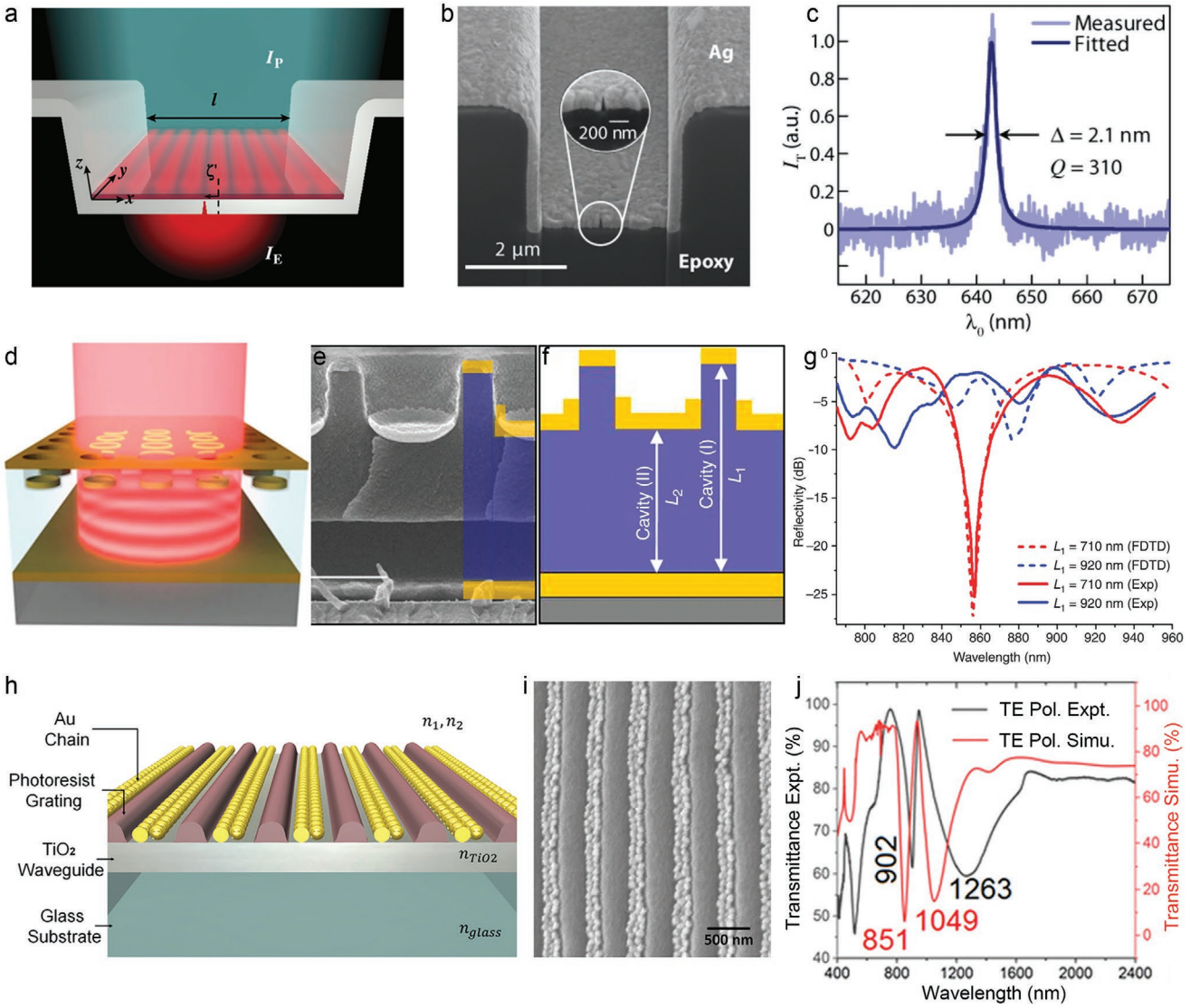

Figure 10. a) Schematic diagram of the plasmonic trench resonator, which consists of two vertical Ag sidewalls and a horizontal floor. The red standing wave represents the trapping of resonant SP modes. The recessed slit can transmit a proportional intensity wave into the far-field. b) SEM image of the fabricated resonator. The width of the slit is 10 nm. c) Measured spectra outcoupled by the slit aperture. The white light illuminates from the open side of the cavity. The measured spectrum was fitted with a Lorentzian shape. d) Schematic illustration of the 3D microcavity structure. e) Cross-sectional SEM of the structure. f) Schematic illustration of a unit cell structure. g) Measured and simulated far-field reflection as a function of wavelength for L_1 = 710 and 920 nm. In the structure, the nanohole period is 740 nm, the diameter is 500 nm, Au thickness H is 200 nm, and $L_2 = L_1 – H$. h) The schematic illustration of the hybrid plasmonic waveguide structure. The grating period is 520 nm, and the thickness is 150 nm. The TiO_2 thickness is 200 nm. i) SEM image of the fabricated hybrid structure in top view. j) Measured and simulated transmission spectra of the hybrid plasmonic waveguide structure. a–c) Reproduced with permission.[147] Copyright 2017, American Association for the Advancement of Science. d–g) Reproduced with permission.[148] Copyright 2011, Springer nature. h–j) Reproduced with permission.[155] Copyright 2019, American Chemical Society.

a guided-mode resonance phenomenon. Moreover, compared with conventional metallic grids, the range of the hybridized guided mode can be extended to mode along the nanoparticle chain lines.

Whispering-gallery modes (WGMs) in dielectric microcavities have been studied extensively owing to their low optical loss and small mode volume.[156] In 2010, Min et al. put forward a plasmonic WG microcavity structure that can couple surface-plasmonic modes and dielectric waveguiding channels.[157] The WG structure is composed of a core silica disk coated with a silver layer, as shown in **Figure 11**a–c. The transmission spectra with different guide gap widths are shown in Figure 11d. The maximum Q-factor value is ≈1400 at phase-matched excitation conditions, close to the theoretical metal-loss-limited. Since WG modes are sensitive to the surrounding environment, they can be used for single biological or chemical molecular detection.[158] However, it needs a tapered fiber waveguide to excite this mode to meet the phase-matching condition. Similarly, the WG structure with an ultrasmall volume has also been investigated to achieve a high-Q factor.[159] In 2019, Su et al. experimentally realized a low propagation loss with a mode area of 0.03 dB μm^{-1} and 0.002 μm^2, respectively, using composite

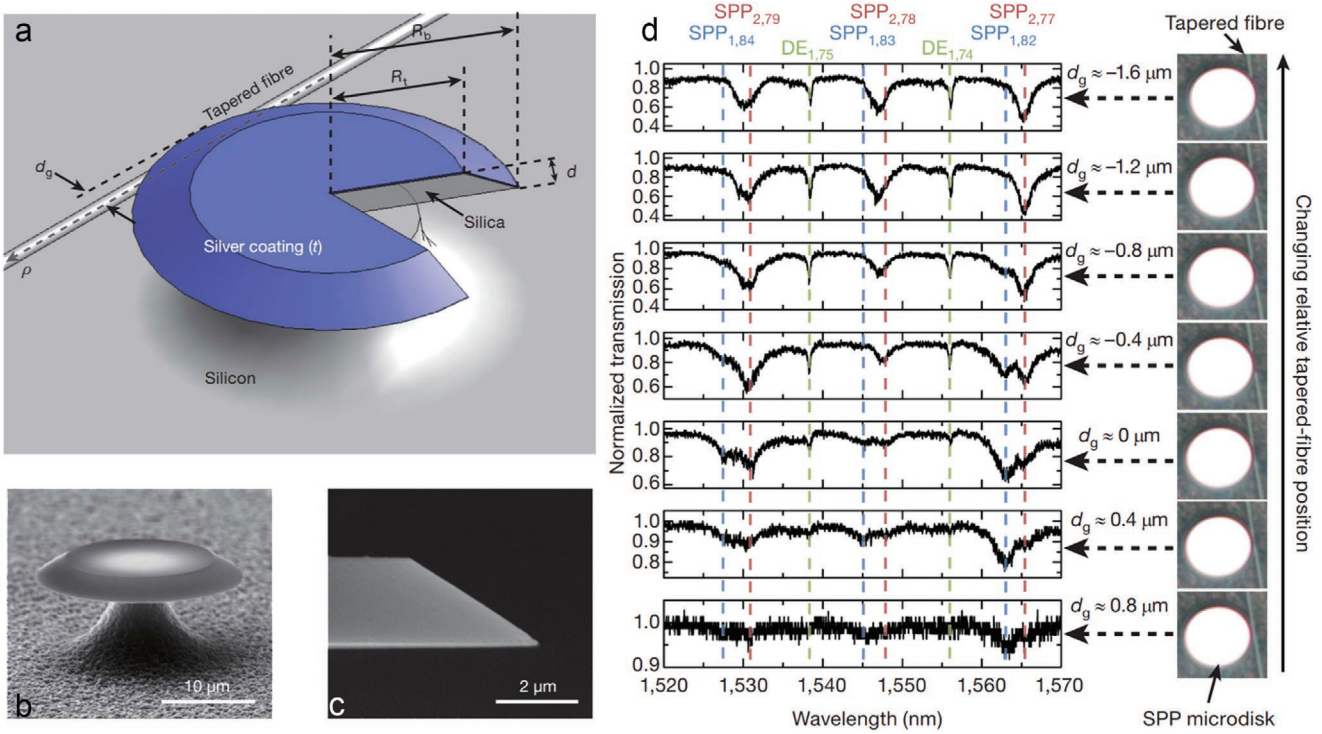

Figure 11. a) Schematic diagram of the whispering-gallery (WG) microcavity structure ($R_b = 10.96$ mm, $R_t = 7.89$ mm, $d = 2$ μm, $t \approx 100$ nm). b) SEM of a fabricated silver-coated SPR microdisk resonator. c) Expanded view of the edge of the SPR microdisk resonator. d) Measured transmission spectrum versus waveguide coupling gap. The gap widths from 0.8 to 1.6 μm. a–d) Reproduced with permission.[157] Copyright 2009, Springer Nature.

hybrid plasmonic waveguides. This structure can also yield a Purcell factor of ≈16 000 due to its low loss.[160]

Graphene can replace plasmonic metals due to its broad tunability and extremely high field confinement in guided resonance.[161] The propagating length of the plasmonic wave in graphene is quite longer than the spatial period of the plasmonic wave, which translates into a high Q-factor for graphene-based guided-mode resonances.[161a] To strongly enhance absorption, graphene can be placed on the dielectric gratings[161c] or embedded in a dielectric layer to form a resonant FP cavity.[161d] Due to the low loss of the dielectric and graphene layer, this guided-mode can realize perfect absorption and achieve a narrow FWHM of 0.5 nm at the midinfrared frequencies. Furthermore, the narrow resonance can be shifted by changing the graphene's Fermi level, which has potential applications in tunable devices. Also, when the graphene is laid on the 1D photonic crystal surface, two peaks with FWHM of 14[161b] and 1.1 nm[161c] can be achieved in the visible and near-infrared wavelength ranges.

For many photonic applications, such as plasmonic photonic circuits, it is critical to confine light at a specific wavelength at a targeted position with a small volume. Moreover, a lower loss indicates a longer propagating distance, essential for practical applications. GMR can be supported by various plasmonic structures, demonstrating remarkable properties of concentrating electromagnetic fields in nanoscale regions achieving subwavelength localization of the guided signals. However, a key challenge is how to efficiently couple to the plasmonic wave because the wave vector is much larger than that of free-space waves. 2D plasmonic graphene materials provide a solution for this problem due to plasmonic oscillations bounded by ribbon rather than propagating plasmonic waves in a continuous graphene layer. Besides, GMRs require precise placement of rationally designed metallic nanoentities on the dielectric gratings, which involves costly processes, such as electron beam lithography.

3.6. Tamm Plasmon Resonances

In 2007, Kaliteevski et al. proposed a plasmon-polariton state that can be formed on the interface between a metal layer and a dielectric distributed Bragg reflector (DBR), which is termed as Tamm plasmon resonances or Tamm plasmon polaritons (TPPs).[28c] In contrast to SP polaritons, TPPs have a zero in-plane wave vector, which can be directly excited and do not require phase-matching. Then, TPPs were the first experimental confirmed by subsequent work.[162] The Bragg mirror has alternate dielectric layers with different refractive indices, which can form a photonic bandgap, and TPPs can be confined in the DBR due to its photonic stop band. The measured transmission and reflection spectra showed an ultranarrow band feature, indicating that TPPs are promising candidates for high Q-factor resonances. **Figure 12** shows a typical structure that supports TPPs, and the simulated reflection spectrum demonstrates a narrow linewidth.[163]

Although the Q-factor of resonance is strongly determined by the optical losses in metal films, the variable DBR

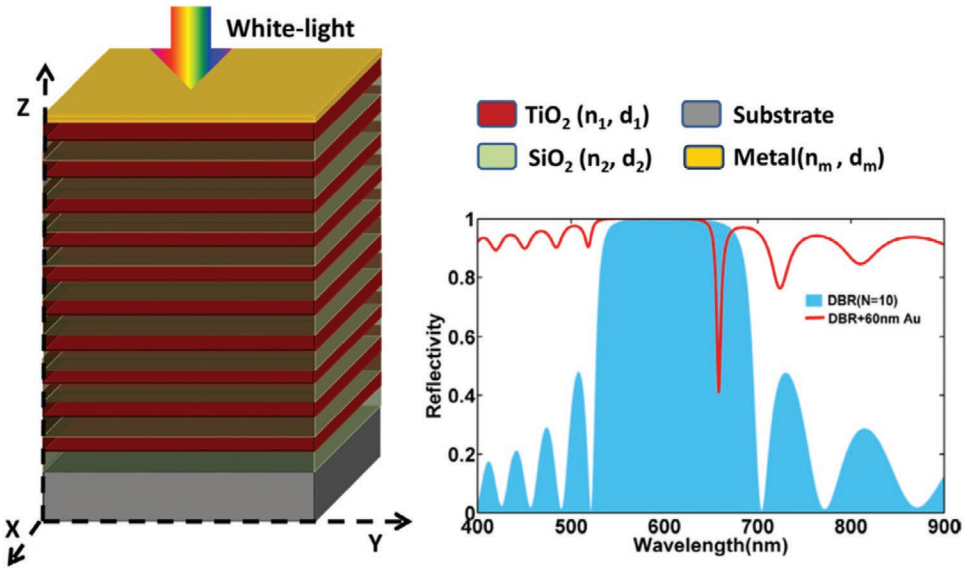

Figure 12. Schematic diagram of the Tamm plasmon system and the simulated reflection spectrum of the bare DBR and "DBR + Au" structures. The Tamm plasmon system consists of periodic multilayer DBR and a layer of the metal structure. The DBR structure has 10-unit cell layers with 1740 nm thickness, and the Au film is 60 nm thickness. Reproduced with permission.[163] Copyright 2018, IOP Publishing Ltd.

characteristics are particularly promising to realizing various high-demand applications. Various common materials for designing DBR structures have been proposed, such as semiconductor materials,[164] all-dielectric photonic crystals,[165] magnetophotonic crystals,[166] epsilon-near-zero materials,[167] etc. For instance, Zhu et al. used a DBR structure combine with a phase-changing material to achieve a narrowband and Q-factor tunable emitter.[168] While conventional TPPs structure has a thin metal layer on a DBR, Yang et al. experimentally demonstrated a structure with a thicker metal layer under the DBR and thus achieved a twice higher Q-factor than that of the conventional one.[56] By introducing a defect layer into the DBR structure, the PIT-like effect has been observed in the TPPs system with an ≈2 nm FWHM at the near-infrared region.[169] Moreover, by embedding 2D materials between DBR and metal film,[170] collective strong coupling,[171] and absorption efficiency[172] arise.

The advantage of the TPPs is that they do not require any 2D or 3D patterning while still maintains a narrow resonant peak, and thus they can mitigate the fabrication limits of 2D or 3D subwavelength structure. Besides, a zero in-plane wave vector indicates that TPPs can be directly excited without the need for nanostructures to couple the incident light. TPPs have demonstrated their implementation in various devices, such as thermal emitter,[56] photodetector,[173] and laser.[174] However, the TPPs usually require periodically grow alternating layers, leading to a relatively thick device. Moreover, the light confinement ability of TPPs is not strong when compared with LSP.

In this section, we have reviewed six plasmonic resonances to realize high-Q plasmonic resonances. These resonance methods provide an essential reference for narrowband spectral applications. It is worth noting that these six modes are not independent of each other. For example, SLR can generate Fano-type lineshape, which is similar to the mechanism of Fano resonance in some cases. Multipolar resonance can couple with SLR to enhance their emission efficiency. PIT can also be viewed as a special case of Fano resonance. GMR can combine with other resonance modes to enhance the Q-factor and spectra intensity. These independent or combined resonance modes provide a variety of options for practical applications. Also, we have summarized some representative work in **Table 1**. The purpose of obtaining high-Q plasmonic resonance is to optimize the performance of devices and improve the performance of various applications. Therefore, different applications need to choose compatible resonance modes and structures. In the next section, we will introduce several typical applications that require high-Q plasmonic resonances.

4. Applications

4.1. Spectrally Selective Thermal Emission

Thermal emission from hot objects usually exhibits broadband features due to the blackbody radiation. A thermal emitter with narrow bandwidth emission property is crucial for achieving-near- and midinfrared thermal sources,[175] spectrally selective infrared thermal detectors,[176] and solar thermophotovoltaics (STPVs).[177] Various designs have been proposed to tailor thermal radiation by using gratings, microcavities, photonic crystals, and metamaterials.[16a,178] In particular, due to the extraordinary optical properties of plasmonic systems, the spectral position, linewidth, and emission efficiency can be easily controlled. Plasmonic structures can provide an ideal way to design spectrally selective thermal emission.

Using the plasmon systems to develop the spectrally selective thermal light sources in the near- and midinfrared region have been developed for many years, such as adopting metalized-surface period lattice structure[179] and MIM multilayer structure.[180] The initial design for the thermal emitter used noble

Table 1. A summary of methods used to obtain high-Q plasmonic resonances.

Resonance mode	Structure	FWHM [nm]	Q-factor	Physical mechanism	Ref.
Surface lattice resonance	$Au/SiO_2/Au$ nanopillar	4.8	147	Reducing radiative loss	[61]
	Au nanoparticles array	≈5	≈150	Suppressing radiative loss	[69]
	Au nanorods array	2	325	Reducing radiative loss	[65]
	Al nanoparticle arrays embedded in PDMS	3.6	≈155	Reducing radiative loss	[79]
Multipolar resonance	Au nanoantennas array	≈68	≈11	Reducing radiative loss	[28b]
	Ag nanorods	≈12.7	≈38	Reducing radiative loss	[95]
Plasmonic Fano resonance	Ag stacked nanoring	8	114	Reducing radiative loss	[258]
	Au nanoslits	3.68	≈359	Reducing radiative loss	[113]
	$Ag/SiO_2/Ag$ asymmetric double elliptical cylinder	8	≈116	Reducing radiative loss	[111]
Plasmonic induced transparency	MIM nanoring/nanorod	≈8	97	Reducing radiative loss	[122]
	Au nanowires embedded in a dielectric slab	0.5	≈1697	Reducing radiative loss	[50]
	multistub resonators	6	≈167	Reducing radiative loss	[133]
Guided-mode resonance	Ag trench FP resonator	2.1	310	Reducing radiative loss	[147]
	$Au/Au/SiO_2/Au$ grating	1.11	≈1410	Reducing radiative loss	[149]
	Ag/SiO_2 WG microcavity	≈1.11	≈1376	Reducing radiative and scattering loss	[157]
Tamm plasmon resonance	DBR/Al nanostructures	≈200	20	Reducing radiative and nonradiative loss	[56]
	$Ag/DBR/Al_2O_3/DBR$ nanostructures	≈2	≈778	Reducing radiative and nonradiative loss	[169]

Au and Ag as plasmonic materials, and they showed narrow emission bandwidth and high-intensity radiation according to Kirchhoff's radiation law.[177] For example, Kady et al. used the Au coated silicon-air photonic crystal surface. It generated the discrete SPR mode at the interface and gave rise to a narrow emission spectrum with a bandwidth of 0.5 μm centered at 4.2 μm.[179] Tsai et al. proposed an $Ag–SiO_2–Ag$ triple-layer metamaterial structure that could suppress the background thermal radiation by the SP coupling, and 0.48 μm of FWHM emission spectra were measured at 300 °C.[180] By changing the structure parameters[181] or elastomeric substrate,[182] different infrared radiation peaks were obtained. Aplasmonic nanochannel structure with U-shaped Au layers has been demonstrated as a spectrally selective thermal emitter with a narrow FWHM of 248 nm.[183] Moreover, Tamm plasmonic structures are also proposed for realizing narrowband thermal emission. Yang et al. used a TPP structure experimentally demonstrated that infrared wavelength-selective thermal emission with an FWHM of 110 nm at 270 °C.[56] Wang et al. designed a hybrid structure by coupling a cavity mode and a TPP mode, as shown in **Figure 13**a, and a narrowband thermal emission was achieved.[184] This hybrid structure exhibited a sharp absorption peak with a 45 nm FWHM at 150 °C, as shown in Figure 13b.

Low-cost metals, such as steel,[185] and Al[186] have also been proposed for thermal emission, which shows a high thermal emissivity in the mid-IR range, and opens up a route for making low-cost thermal emitters. The working temperature of spectrally selective thermal emission is usually above 1000 K. However, Au and Ag have relatively low melting points, and their melting points quickly decrease as the metal size shrinks to the nanoscale.[15a] This imposes restrictions and challenges for appliactions requiring high temperatures. Refractory metallic nanostructures (such as W, Mo, Ta, ZrN, TiN, etc.) have been proposed as heat-assisted applications.[187] The refractory plasmonic materials exhibit excellent plasmon characteristics and high-temperature stability, providing a solution for the thermal emission. For example, TiN is a typical refractory plasmonic material and used as a narrowband emitter material.[188] Wang et al. proposed a TiN-based stack metamaterial structure, which could integrate plasmonic absorber and emitter, and a 0.6 μm bandwidth emission was achieved by numerical simulation.[189] Jiang et al. also designed a TiN-based nanocavity structure that encapsulated by different dielectrics, and it showed an excellent spectrum selectivity and high-temperature stability (at 1073 and 1273 K for 2 h).[190] Molybdenum (Mo) also shows unique plasmonic properties with high thermal stability. Yokoyama et al. used a $Mo–Al_2O_3–Mo$ structure, which can operate at 1000 °C for 3 h with a narrowband emission.[191] Tungsten (W) is usually chosen as the emitter material due to its high melting point (3695 K) and excellent corrosion resistance. However, the W-based emitter often has a broad emittance spectrum because the intrinsic spectral selectivity of tungsten is poor.[192] However, low cost, and large area selective thermal emitters with a narrow band resonance can be realized by coupling the W-based emitter layer with TPPs mode.[193]

An extremely essential application of spectrally selective thermal emission is solar thermophotovoltaics (STPVs). Photovoltaics (PVs) is a common method to convert solar energy into electricity.[10] However, due to the mismatch between the incident photon energy and the bandgap of the solar active material, the energy conversion efficiency of single-junction PV cells is subject to the Shockley–Queisser (SQ) limit. STPV has a higher theoretical power conversion efficiency than the conventional single-junction solar cell, overcoming the SQ limit.[194] The performance of STPV relies on several intermediate energy conversion steps: the heat generated from a light absorber is conducted to the emitter that radiates thermal energy. Afterward, the thermal energy is converted to electricity

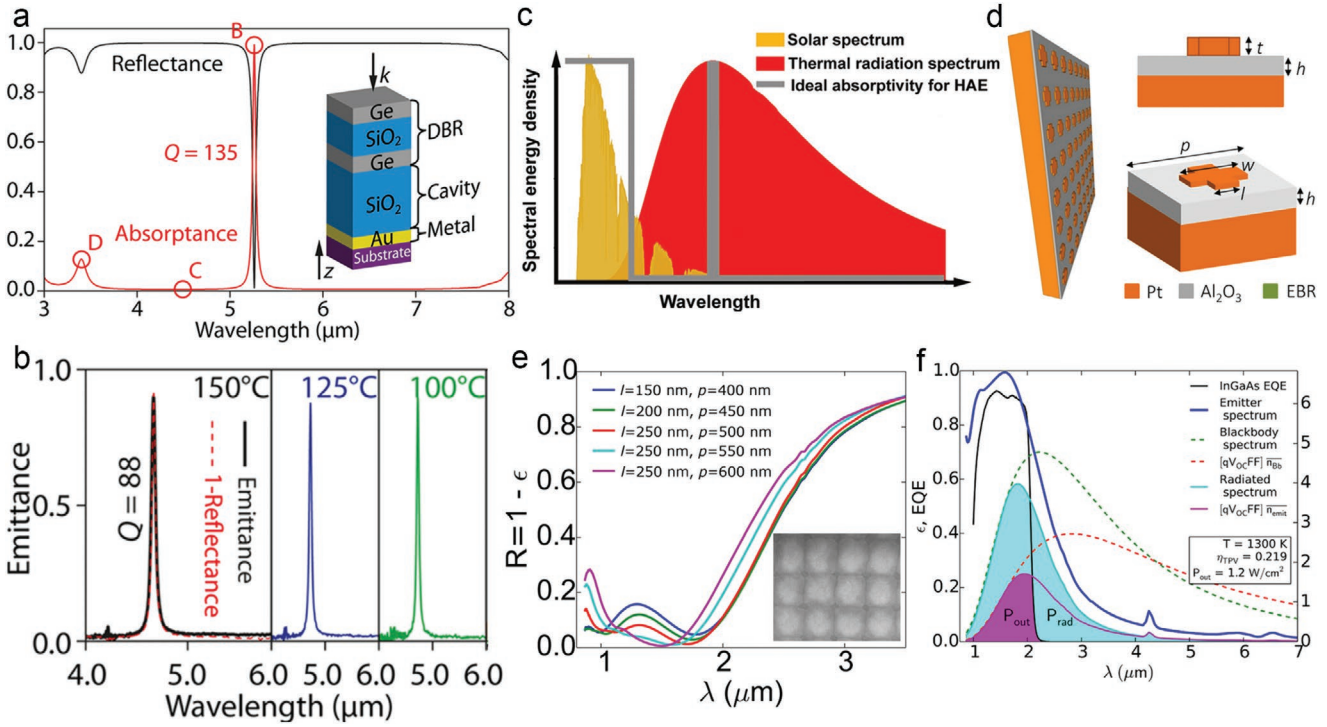

Figure 13. a) Schematic diagram of the Tamm plasmon structure and the simulated reflectance (black solid curve) and absorptance (solid red curve) spectra. The DBR used the Ge/SiO_2/Ge structure. b) Calculated emittance spectra at different temperatures (100, 125, and 150 °C). c) Ideal spectral selectivity of the hybrid absorber–emitter (HAE). d) Schematic diagram of the MIM metasurface structure emitter, which consists of a platinum (Pt) cross above a Pt substrate, an Al_2O_3 spacer layer, and a layer of Al_2O_3 encapsulation on the substrate. e) Simulated and experimental reflectance spectra with the encapsulated Al_2O_3 layer on the surface. The deposited Al_2O_3 layer is 150 nm thick. f) The model of selective emitter-TPV system at 1300 K. Those lines show the black body power, normalized photon density, radiated power, radiated photon density, and the emissivity spectra. a,b) Reproduced with permission.[184] Copyright 2018, American Chemical Society. c) Reproduced with permission.[257] Copyright 2018, Wiley-VCH. d–f) Reproduced with permission.[198] Copyright 2014, AIP Publishing LLC.

via a PV cell.[177] Since the radiation spectrum of the emitter is broad, and it mismatches the bandgap of the PV cell, much of the radiation energy is wasted. In order to make the process efficient, the spectrally selective emitter should have a large emittance for photon energies higher than the bandgap of the PV cell, and a small emittance for photon energies less than the bandgap energy.[195] The ideal spectral selectivity of the narrowband infrared emission spectrum can be seen in Figure 13c. The ideal selective emitter would emit only photons with energy equal to the bandgap energy of the PV cells at elevated temperatures. Generally, STPV requires a working temperature of at least 1000 K.[196] In order to elucidate these constraints, various selective thermal emitters have been put forward to improve the STPV conversion efficiency. Besides, the refractory plasmonic metals can be used in STPV systems. Epsilon-near-zero (ENZ) material, such as Al-doped ZnO, can be used in the spectral selectivity to reduce sub-bandgap losses at high temperature.[197] Depositing a protective layer on the noble metals can also increase the operating temperature while maintaining performance. For example, platinum (Pt) has been demonstrated to be used in an STPV system. It could survive at 1300 K when encapsulated in an Al_2O_3 layer.[198] Figure 13d shows the designed structure of the metasurface emitter. The reflectance spectra in Figure 13e shows that its emissivity matched to the external quantum efficiency spectrum of InGaAs PV material, as demonstrated in Figure 13f, and an optical-to-electrical power conversion efficiency of 22% was achieved.

In summary, it has been shown that spectrally selective thermal emission can be used in the near- and midinfrared thermal sources and STPV devices. Thermal emission based on SPRs yields sharp emission peaks, but they are vulnerable to angular dependence and a poor emittance at high temperatures, leading to impaired intensity and sharpness of resonances. It can be theoretically predicted that these applications have extremely high performance. However, there remain gaps between the theoretical design and the experimental realization because it is challenging for emitters to simultaneously meet the requirement for high emittance, narrow bandwidth, angular or polarization insensitivity, and cheap nanofabrication steps.

4.2. Sensors with High Sensitivity

Plasmonic sensors can be used to detect changes in surrounding materials. When chemical or biological species interact with the sensor surface, the dielectric environments change can cause local electromagnetic (EM) fields and SPR shifts. High-Q plasmonic sensor is desired because it means that more light can interact with surrounding materials rather

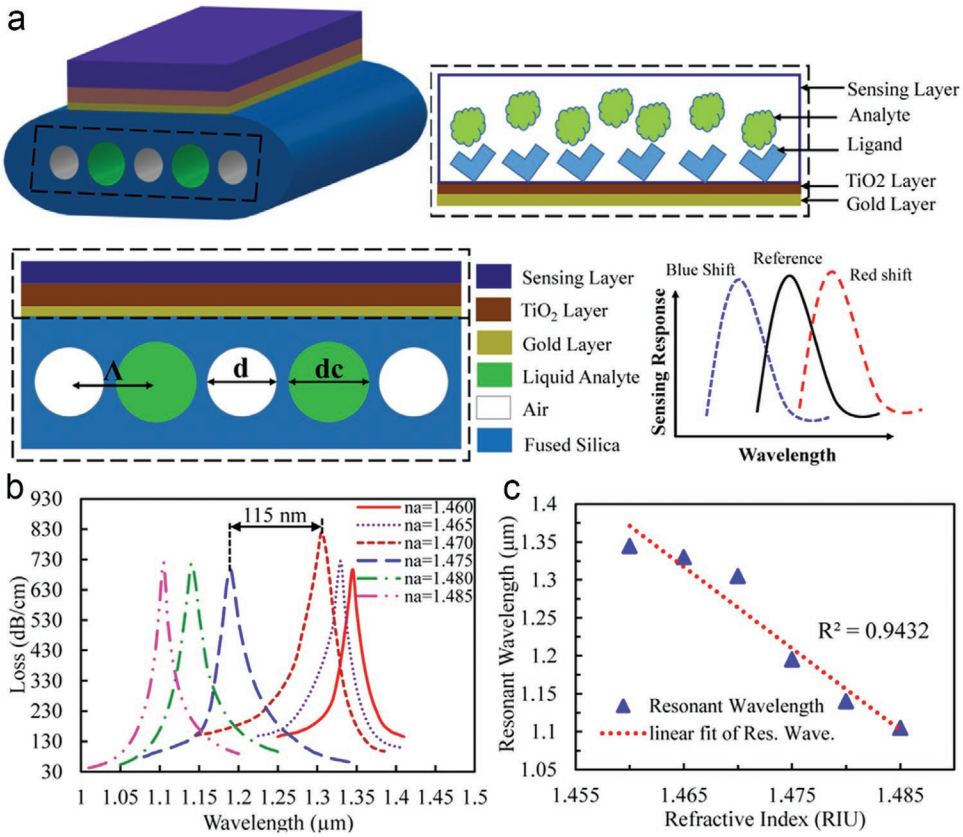

Figure 14. a) Schematic diagram of the proposed multicore flat fiber sensor in the 3D model, which consists of five airholes where two of them are filled with the high refractive index liquid. Besides, the Au layer, TiO_2 layer, and sensing layer are arranged sequentially on top of the sensor surface. The ligands attached with the TiO_2 layer and analyte will flow through the sensing medium and bond with the ligands, resulting in the shift in resonance peak. b) Loss spectrum with varying analyte refractive index from 1.46 to 1.485. c) The linear fitting of resonant wavelength versus analyte RI. a–c) Reproduced with permission.[205] Copyright 2016, Optical Society of America.

than being wasted via losses and has advantages on amplitude noise and spectral resolution. Usually, the refractive index sensitivity ($S = \Delta\lambda_p/\Delta n$) can be characterized by the peak shift per refractive index unit (nm RIU^{-1}). Hence, a figure of merit (FOM = S/FWHM, or FOM* = max ($dI(\lambda)/dn(\lambda)/I(\lambda)$)) can be defined to evaluate the performance of the sensing capabilities, where S stands for refractive index sensitivity and $dI(\lambda)/I(\lambda)$ is a relative intensity change at a fixed wavelength λ.[199] To increase the FOM of the plasmonic sensors, one can choose to either increase the S or reduce the resonance linewidth.

Liu et al. first experimentally demonstrated a plasmonic sensor using a perfect absorber in the near-infrared regime.[200] The sensor consists of an Au disk array, an MgF_2 dielectric layer, and an Au bottom layer. A FOM* of ≈87 was achieved by detecting the intensity changes under different dielectric materials (air and water). Following this work, metal nanoparticles,[201] metamaterial,[150] and all-metal plasmonic absorber[75] have been designed for sensors via using SLRs,[202] multipolar resonance,[201] Fano resonance,[203] PIT,[116] gain-assisted resonance,[204] etc. Due to the coherent interference between radiation and subradiation modes, Fano resonances and GMRs are more sensitive to trace the change of the refractive index. A maximum sensitivity of 23 000 nm RIU^{-1}, using GMRs, has been achieved by the fiber-based sensors.[205] **Figure 14**a shows the schematic diagram of the sensor, where the sensing layer and metallic layer are placed outside of the fiber structure; the fiber structure consists of five airholes for light guiding and to optimize the evanescent field, which can be used to improve the sensitivity of the sensor. The small change of the refractive index in the analyte can cause the change of phase-matching wavelength and raise the resonant spectrum shifts, as shown in Figure 14b. Furthermore, the sensor shows a high linear sensing response between the refractive index and the resonant wavelength, as shown in Figure 14c. Yu et al. proposed a sensor based on the hybrid plasmonic–photonic crystal, demonstrating an atomic layer sensitivity.[55] The hybrid plasmonic–photonic sensor consists of a close-packed monolayer of polystyrene colloids self-assembled on a chemically modified gold surface, as shown in **Figure 15**a. To demonstrate its high sensitivity under atomic layer resolution, they deposited Al_2O_3 with different thicknesses on the sensor surface via different deposition methods, as shown in Figure 15b,c. Also, they proposed a modified empirical FOM because the traditional FOM did not properly represent the real situation of surface-based sensing. Besides, they demonstrated that the sensor has the gas phase sensing capability by detecting the physisorption of ethanol on the sensor surface, as shown in Figure 15d. The amount of ethanol physisorbed on the surface of the sensor can

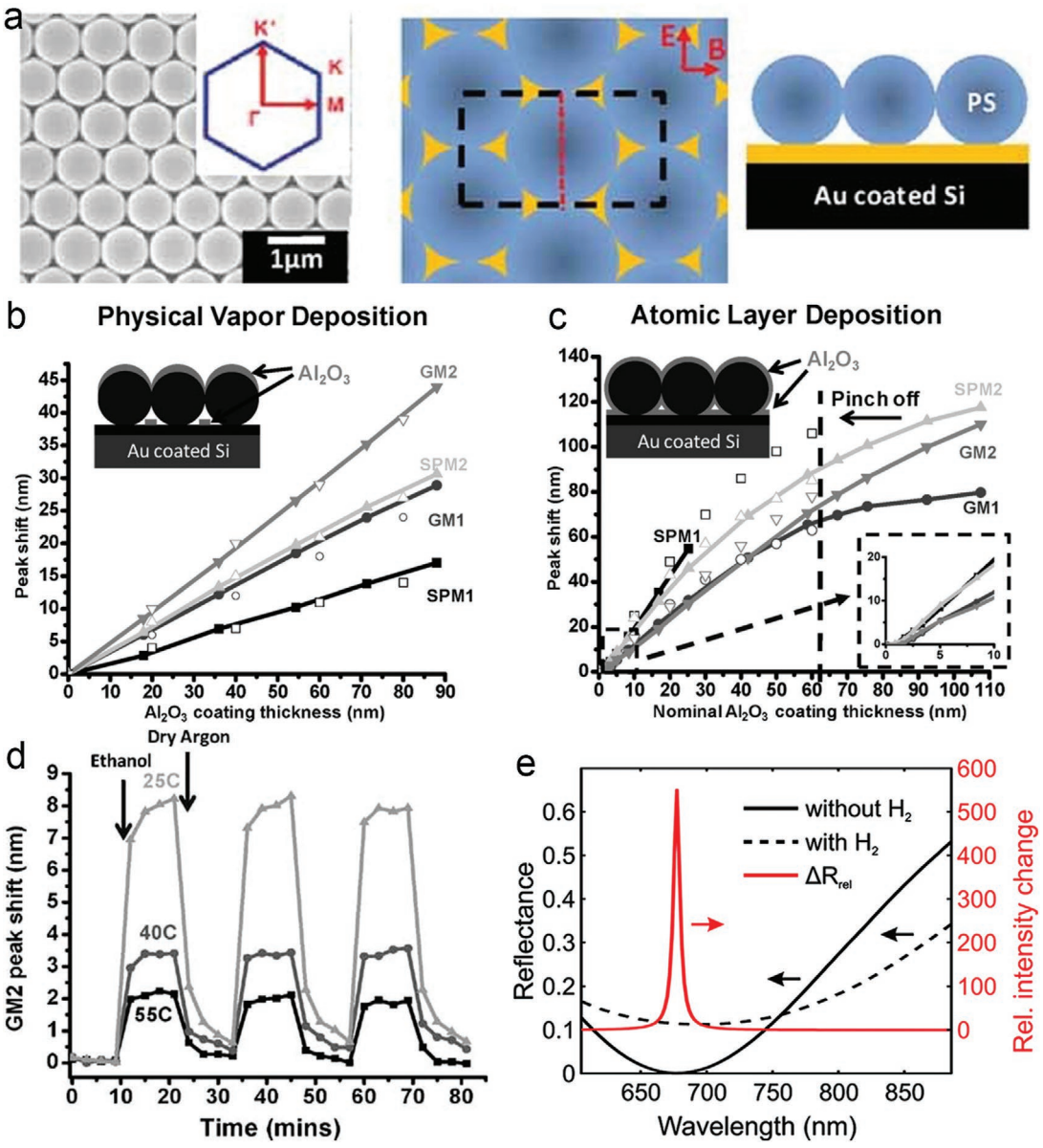

Figure 15. a) Schematic of the structure with top-view SEM image, top-view schematic, and side-view schematic, from left to right. b) Reflection spectra peak shift versus Al_2O_3 coating thickness in the case of physical vapor deposition and c) atomic layer deposition. d) Peak shift from the dry argon state to ethanol saturated argon at 25, 40, and 55 °C. e) Simulated response of the sensor structure to hydrogen exposure. a–d) Reproduced with permission.[55] Copyright 2010, Wiley-VCH. e) Reproduced with permission.[209] Copyright 2011, American Chemical Society.

be determined by measuring the peak shift. The hybrid plasmonic–photonic mode can also be excited under oblique illumination. Liu et al. demonstrated a high spectral Q-factor of 1375 using a hybrid plasmonic–photonic mode under oblique illumination.[206] Liu et al. also designed a sensor using the plasmonic–photonic mode to show an extremely narrow FWHM of 3 nm. The sensor exhibited excellent sensitivity for detecting biomolecules, with a FOM value of 730.[207] Chen et al. proposed a plasmonic waveguide system—they used a metal nanowire-on-mirror setup—to probe subpicometer resolutions. It largely exceeds the theoretical maximum vertical resolutions of scanning probe microscopes, and they demonstrated its potential use in some ultrasensitive sensing applications.[208]

While some sensors use the peak shift to detect changes, others detect the changes by observing intensity changes resulting from the adsorption of the target molecule. For example, Tittl et al. used palladium-based plasmonics to measure the hydrogen concentrations.[209] As the gas concentration increases, the spectral shift and reflection intensity increase, as shown in Figure 15e. Besides, high-Q sensors have the potential to realize the direct detection of a single monolayer of biomolecules in the naked eye,[210] molecular vibrational spectroscopy,[211] explosives detection,[212] and plasmonic colors.[213]

In summary, numerous plasmonic nanostructures have already been developed as signal amplifiers and transducers

for optical sensing by utilizing various modes to narrow the linewidth of plasmonic resonances, holding promise for biomedical, food sciences, chemical or toxic compound detection, environmental monitoring, pharmacy, and industry. Increasing field intensities is the most common way to boost plasmonic biosensing performance, but there is a tradeoff due to the photodamage of biological specimens.[214] Future challenges of the plasmonic sensors are the development of low-cost platforms, designing devices that can detect target molecules in complex fluids, and reusability.

4.3. Single-Photon Sources with Boosted Purcell Effect

For optics-based quantum information processing technologies, single-photon sources are key components in quantum devices and quantum communications.[215] The ideal single-photon source should deliver photons one by one, emitted at any arbitrary time, in a pure quantum state, and high efficiency.[216] An essential research direction of single-photon sources is to use the Purcell effect to enhance the spontaneous emission rate, shorten the radiative lifetime, and achieve strong coupling.[217] Plasmonic nanostructures have been proved to significantly increase the emission rate due to the presence of local density of states (LDOS). In the weak coupling region, the enhancement can be characterized by the Purcell factor ($F_p = (3\lambda^3/4\pi^2)(Q/V)$). It includes two main quantities: the modal volume (V) and the Q-factor.[218] High-Q factor and small V are highly desirable for increasing the brightness of the quantum emitters. Compared with photonic crystals, plasmonic nanostructures have huge field enhancements, a small mode volume due to the light confinement.

Initially, a nanowire was used to support surface plasmons by coupling with a quantum dot at the wire end—it can form a simple two-level system to enhance the quantum dot spontaneous emission.[2a] However, it is challenging to direct the photons to specific channels. By coupling the emitter with 1D nanoparticle chains, unidirectional single-photon sources can be achieved.[219] Besides, one can combine different single quantum emitters, such as QD,[220] nitrogen-vacancy,[221] with plasmonic structures to achieve highly bright single-photon sources.[222] For example, Choy et al. presented an approach that directly embeds single nitrogen-vacancy centers into plasmonic nanostructures, in which the mode volume is 0.07 $(\lambda/n)^3$, and the Q-factor is 10.[223] Also, Al can be used to replace traditional Au or Ag materials for Purcell enhancements. For example, Tobing et al. designed an Al dimer antenna with an ≈10 nm gap structure for polarization resolved photoluminescence enhancement. A much smaller mode volume of 2.1×10^{-3} $(\lambda/n)^3$ was achieved, and the corresponding Purcell factor can reach ≈104.[224] Moreover, the semiconductor material can be integrated with plasmonic materials to form a resonant plasmonic nanocavity and generate hot-exciton emission.[225] As shown in **Figure 16**a, by combining microcavities and plasmonic antennas, one can achieve a stronger emission rate with a much boosted Purcell effect than the cavity or antenna alone.[226] By theoretical calculation, this coupled system can strongly boost emission enhancements—an enhancement

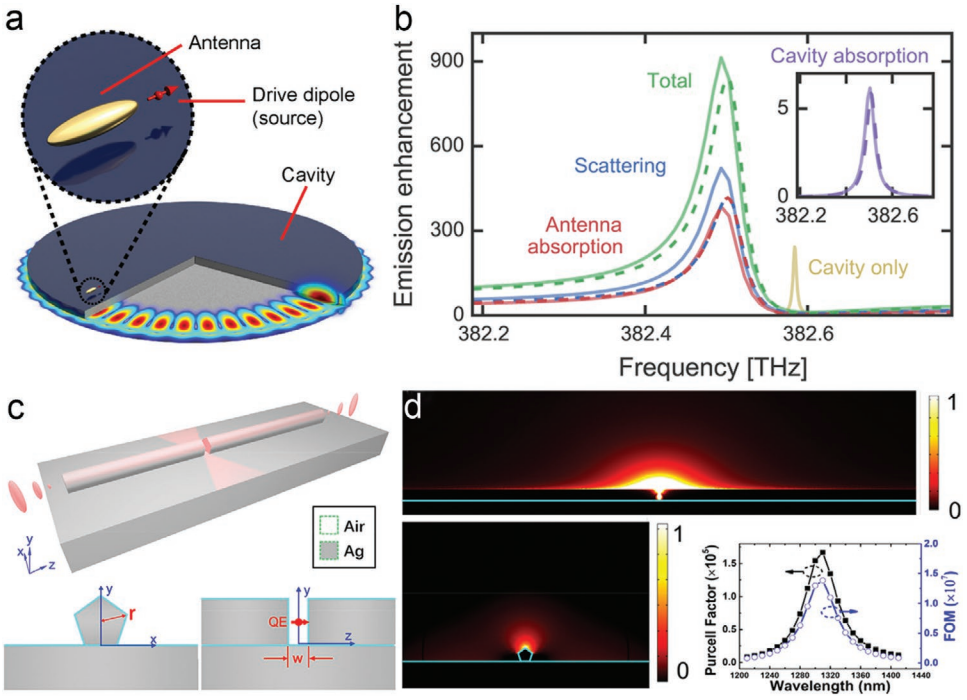

Figure 16. a) Schematic diagram of the coupled cavity–antenna system, which is driven by a dipolar source. The cavity supports a whispering gallery mode shown in the cut-out. b) Emission enhancements in a hybrid system from the oscillator model (dashed) and from simulations (solid). c) Schematic diagram of the plasmonic waveguide-slit structure on the silver substrate. d) Power flow distribution of the proposed structure. (Bottom right) Purcell factor and FOM varying with a different wavelength in the proposed structure. a,b) Reproduced with permission.[226] Copyright 2016, American Chemical Society. c,d) Reproduced with permission.[231] Copyright 2019, Wiley-VCH.

factor of ≈914 was achieved, which is a significant increase with respect to the bare cavity (242) and antenna (≈65 near cavity resonance), as shown in Figure 16b.

It has been experimentally demonstrated that guide-mode plasmonic nanostructures can largely enhance the spontaneous emission rate.[227] MIM waveguides have the potential to provide the smallest mode cavity, thus enabling a large Purcell factor.[228] Akselrod et al. demonstrated an Ag nanocube with a MIM structure with a large emission rate enhancement.[229] The giant field enhancement appeared in the dielectric gap region, and a maximum Purcell enhancement exceeded 1000 with a high quantum efficiency greater than 0.5. Subsequently, Luo et al. used carbon nanotubes coupled with MIM nanocavity arrays, and they obtained a Purcell factor of 180 and Purcell-enhanced quantum yields of 0.62.[230] Recently, Zhang et al. designed a plasmonic waveguide-slit structure that consists of an Ag nanowire slit and Ag substrate, as shown in Figure 16c.[231] The electromagnetic field is confined at the slit and Ag substrate, and it provides a large selection range to support the resonant mode in the nanoslit, as shown in Figure 16d. As a result, the Purcell factor of $F_P = 1.68 \times 10^5$ was predicted due to a large FOM of $\approx 2.0 \times 10^7$.

Besides, other plasmon resonance modes have been reported to enhance single-photon emission. For example, Tran et al. proposed a hybrid system that used quantum emitters in 2D hBN materials integrated with SLR structure to achieve enhanced single-photon emission, as shown in **Figure 17**a.[232] SLR structure offers a high-Q and low-loss cavity in the red spectral region, and an FWHM of 50 nm was obtained, as shown in Figure 17b. The coupled emitters exhibit a 2.6 fold enhancement of photoluminescence (PL) and a reduced fluorescence lifetime of 0.27 ns. The emitter is an SPE with nonclassical light emission, as a $g^2(0)$ value of 0.29 shown in Figure 17c. Moreover, QDs coupled to a Tamm plasmon mode also designed for single-photon emission.[233] The designed structure is shown in Figure 17d, and the PL emission spectra of the device as a function of the excitation power is shown in Figure 17e. The QD exciton line experiences an acceleration of spontaneous emission with a radiative lifetime of 450 ± 100 ps. Photon correlation measurements curve $g^2(\tau)$ is shown in Figure 17f, in which a $g^2(0)$ of 0.35 ± 0.1 can be observed. The structure provides a simple nanoprocessing tool for accelerated single-photon emission. Besides, Tamada et al. demonstrated that high-order SPR mode could also be coupled to enhance Purcell emission with QDs emitter.[234] In the past decade, using the plasmonic cavity mode to boost the Purcell effect has made significant progress. It provides a new way to generate high pure and indistinguishable single photons with high prospects of realizing important applications in quantum optics, bioimaging, and quantum engineering in the near future. However, to meet the practical application, brightness,directivity, indistinguishable, full

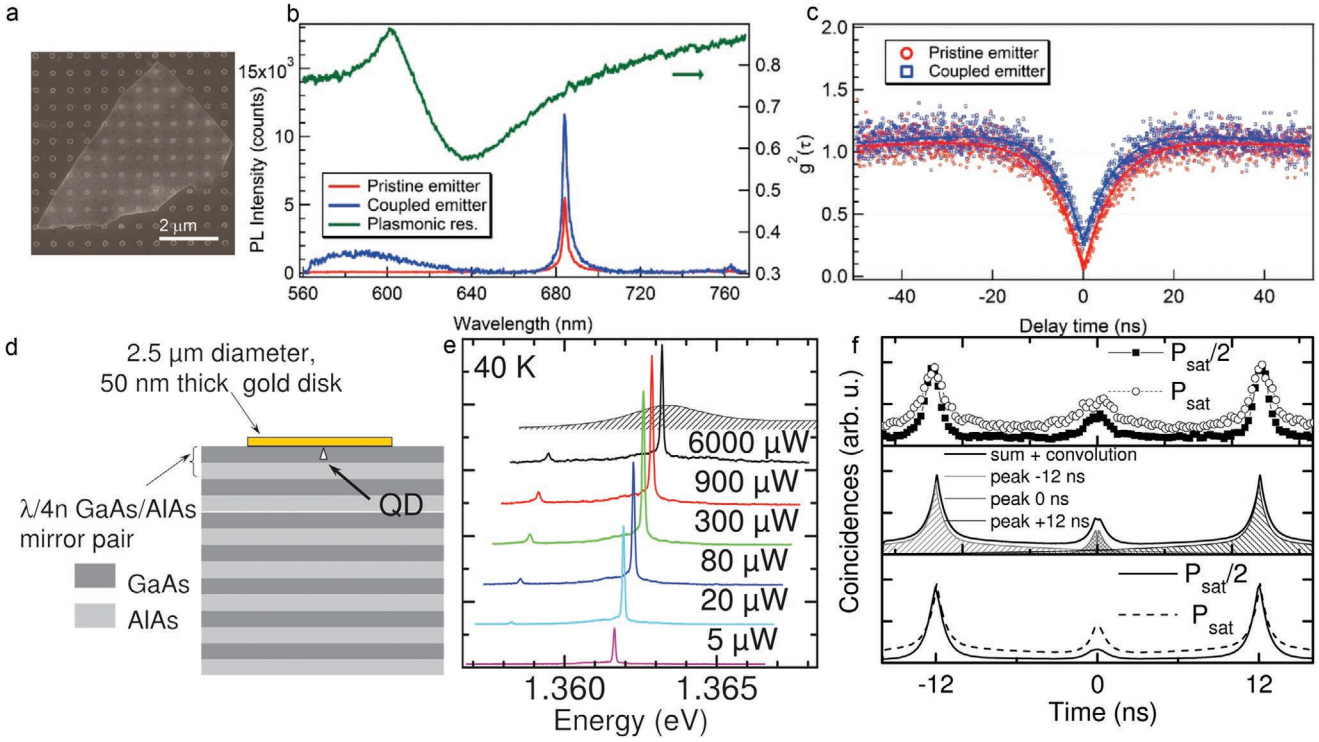

Figure 17. a) The SEM image of a hybrid quantum 2D material system integrated with an Ag nanoparticle array on a silica substrate. The lattice period is 400 nm. b) The measured PL spectra of a pristine (red curve) and coupled (blue curve) single-photon emitter and transmission spectrum of the lattice (green curve). c) Second-order autocorrelation functions, $g^2(\tau)$, obtained from the pristine (red circles) and coupled (open blue squares) system. The $g^2(0)$ values for emission from pristine and coupled emitters are 0.06 and 0.29, respectively. d) Schematic of the confined Tamm plasmon structures for single-photon extraction. The sample is cooled down to 40 K for the measurement. e) PL spectra of the device for increasing excitation powers. f) Measured and calculated autocorrelation function $g^2(\tau)$ for two excitation powers. a–c) Reproduced with permission.[232] Copyright 2017, American Chemical Society. d–f) Reproduced with permission.[233] Copyright 2012, American Institute of Physics.

scalability, and long-wavelength high-Q single photons are essentially desired.[235]

4.4. Plasmonic Filters

Plasmonic filters have extensive applications in displaying, detecting, printing, and decoration, etc.[236] Narrow linewidth, high transmission efficiency, wavelength tunability, polarization-insensitivity, and minimized size are desirable for plasmonic filters. By using plasmonic nanostructures, photons, and plasmons can be converted to each other, offering a new solution to traditional optical processes such as color filtering and spectral imaging.[237]

High Q-factor resonance paves a way to achieve high-resolution spectral imaging because of their relatively narrow transmission passband. For example, Xu et al. used MIM waveguide geometry to design a color filter to filter white light into a single color.[17b] The design provides an absolute transmission over 50% and FWHM about 100 nm at given three colors. **Figure 18**a shows seven square-shaped plasmonic color filters with different stack period.[17b] Miyamichi et al. fabricated a silver-film plasmonic filter with concentric periodic corrugations, as SEM images are shown in Figure 18b,c.[238] By changing the corrugation periods, the light at specific wavelengths can be transmitted through the aperture at the center. The measured transmission spectra from visible to the near-infrared range and microscope images are shown in Figure 18d ,e. This design is expected to realizemultispectral imaging. By using plasmonic resonance with a high Q-factor, one may further improve the resolution of the imaging. When a filter's FWHM is less than 30 nm, the imaging systems can filter more than 20 colors from visible to the near-infrared spectrum, constructing the optical spectrum at every pixel in an image.[236b] High spectral resolution plasmonic color filters have been designed with the narrow band-pass transmission (<30 nm).[239] Wu et al. proposed a cavity resonator coupled with bus and drop waveguides. A narrow linewidth with an FWHM of 7 nm spectrum was obtained, and it provides a way to design optical logical devices.[17a] The integrated single-color plasmonic filter can be served as a CMOS image sensor, as shown in Figure 18f.[240] The back-illuminated microscope images show the filter is extremely robust to period and diameter. Compared with the single-color plasmonic filter, multispectral filters can be used in signal processing and communications,[241] which can convey more information than a single band. Double band,[242] triple band,[243] and multiple bands[126] have been designed for plasmonic filters.

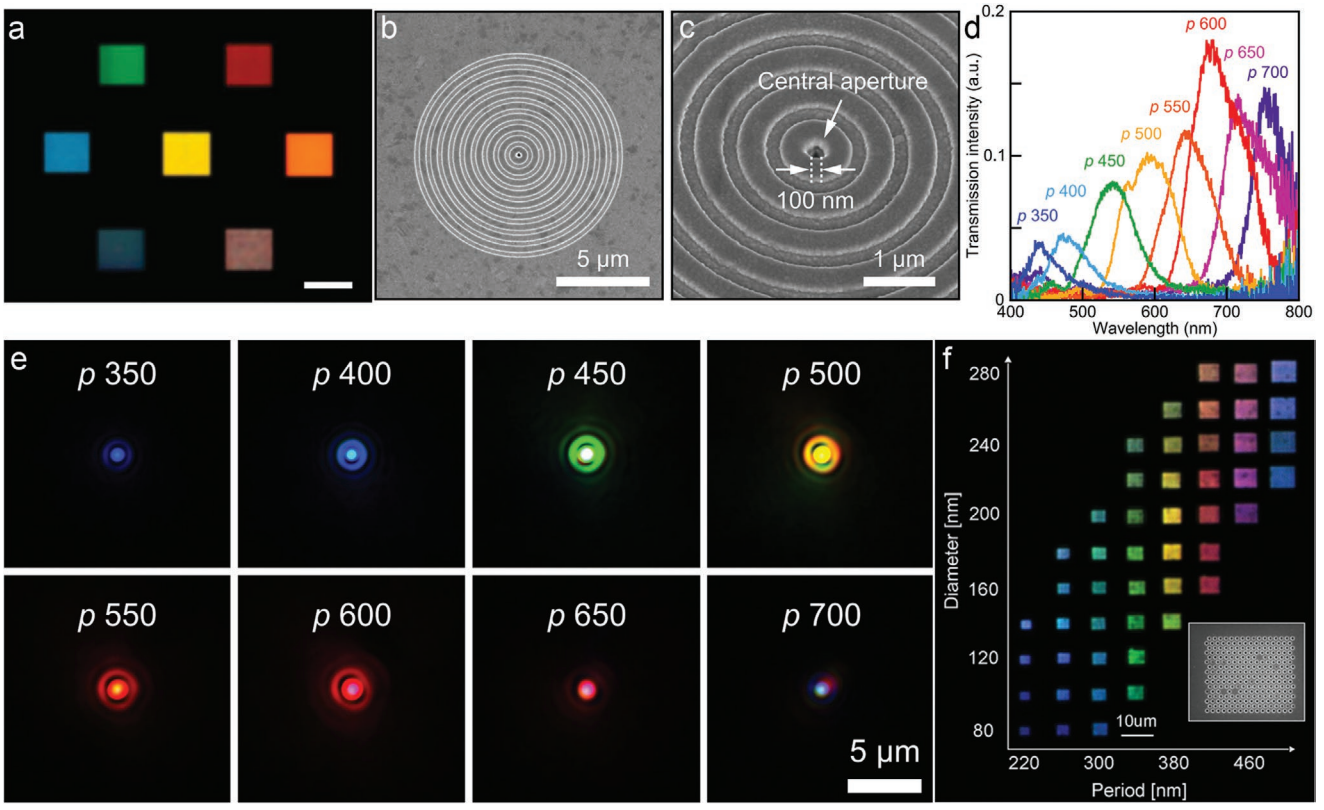

Figure 18. a) Optical microscopy images of seven plasmonic color filters illuminated by white light. Scale bar, 10 μm. b) SEM image of the fabricated plasmonic color filter (top-view). Nine grooves with a period of 600 nm were concentrically fabricated around the sub-wavelength aperture. c) Bird's eye view SEM image. The sub-wavelength aperture about 100 nm in diameter, and concentric periodic corrugations were fabricated on a silver thin film. d) Measured transmission spectra for each filter with a different period from 350 to 700 nm. e) Optical microscope images of the plasmonic color filter with different period shown in (d). f) Back-illuminated microscope images of the fabricated hole array filters. (Inset) SEM image of a representative hole array filter. a) Reproduced with permission.[17b] Copyright 2010, Springer Nature. b–e) Reproduced with permission.[238] Copyright 2018, Optical Society of America. f) Reproduced with permission.[240] Copyright 2012, American Chemical Society.

Compared with traditional optical filters, plasmonic filters have many advantages, such as higher reliability under long-term exposure at high temperatures and/or ultraviolet irradiation.[240] Also, the transmission wavelength and polarization can be easily controlled,[244] and the device is much thinner and easy to be fabricated.[236a] These features of plasmonic filters have shown huge potential for industrial applications. The plasmonic filters have particular usages on spectral analysis, such as gas sensing, disease diagnosis, and security monitoring. Plasmonic RGB filters have demonstrated their potential to replace the organic color filter in digital cameras. However, transmission efficiency needs to be further increased.

4.5. Plasmonic Band-Edge Laser

Compared with conventional lasers, plasmonic nanolasers can support ultrafast dynamics and ultrasmall mode volumes, and they have been widely used in optics and biological applications. However, they contest heavy losses, including Ohmic loss, radiation loss, and scattering loss, etc. The Q-factor of the plasmonic lasers is lower than that of their photonic counterparts. However, plasmonic lasers have many advantages when the laser size is shrunk to or below the diffraction limit. High-Q plasmonic resonances can assist plasmonic nanolasers in resolving these issues. Single-band edge states can trap light, and the LDOS can be enhanced near the band edges due to the reduced group velocity. The modified LDOS can strongly increase not only spontaneous emission rates but also stimulated emission processes, leading to boosted laser modulation speeds with low-threshold lasing.[19a,245] Also, Band-edge modes with low group velocity can boost the light-matter interaction with gain materials, and thus allowing for the compensation of the loss of SP at band edge modes.

Due to the extremely small mode volumes and high optical field enhancement, plasmonic crystals, such as metal hole arrays,[246] nanodisk arrays,[247] and bowtie dimers arrays[248] have been reported for nanoscale band-edge lasing. For example, Zhou et al. used 2D Au nanoparticles arrays on a glass substrate covered by an organic gain medium to make a plasmonic band-edge laser, as shown in **Figure 19**a.[249] The calculated extinction of band-edge lattice plasmons agreed with emission spectra, as shown in Figure 19b,c. The stimulating energy can be transferred from the gain to the band-edge lattice plasmons because the SLRs sustain a large LDOS. In the plane of the nanoparticle arrays, a standing wave can be formed at the edge of nanoparticles with dipole–dipole coupling, and the stimulated emission can be generated in these optical enhancement fields with pump pulse. As a result, a lasing linewidth <1.3 nm and 200-fold enhancement of the spontaneous emission rate was achieved. The lasing action can be tuned in real-time by changing the solid gain materials into liquid based on band-edge lattice plasmons.[250] The lasing direction mentioned above is bidirectional, and thus half the emitted light is wasted. By combing the nanoparticle arrays and metal film, Yang et al. designed a unidirectional emission lasing.[251] Grouping a single 2D array of nanoparticles into microarrays, multiple mode band-edge lasers were achieved—it can precisely control the wavelength and spectral separation of the multiple mode lasers.[19b] One can conclude that nanoparticle arrays that support SLRs are ideal structures for band-edge lasing because they not only have a high Q-factor and localized field enhancement around the nanoparticles but can also slow light at the SLR band-edge with a standing wave.[252]

The major advantages of band-edge lasing are low threshold and narrow emission linewidth. In general, plasmonic lattices can support dark and bright SLR modes. The dark modes can have a higher Q-factor, which is convenient for lasing compared to bright modes. Hakala et al. demonstrated that band-edge lasing in both dark and bright modes are feasible. The dark mode has a higher emission intensity, a lower lasing threshold, and a narrower linewidth than the bright mode.[253] Guo et al. studied the lasing at *K* points of the Brillouin zone in a honeycomb plasmonic lattice.[254] The energies of diffracted orders are shown with dashed lines in Figure 19d, which can determine the existence of a lasing mode at ≈1.44 eV (mode A_1'). By comparing the real-space images with dipole orientations, it further confirms that the systems can lase in the singlet mode A_1'. Figure 19e shows that the singlet A_1' has an energy minimum at the *K* point. Thus, the lasing action confirms that band-edge emission enables the minimum excitation threshold. Recently, an ultralow-threshold continuous-wave band-edge laser has been proposed.[255] Figure 19f shows the schematic of the plasmonic lasers—it used Yb^{3+}/Er^{3+}-co-doped gain materials coated on Ag nanopillar arrays to lower the lasing threshold. A threshold of 70 W cm^{-2} was obtained at room temperature, orders of magnitude lower than other small lasers. This low-threshold band-edge laser opens possibilities for integration of low-power circuits as well as in vivo applications.

Recent progress in plasmonic band-edge lasing paves the way to achieving engineered nanolasers with deep subwavelength mode volumes and low threshold. This simple system provides rich properties for smaller lasers and provides a bright future for open challenges that required multiple materials and are restricted to the conventional diffraction limit. Although some research groups have demonstrated experimental results on plasmonic band-edge lasing, their experimental condition requirements are very demanding. Besides, one should conquer the temperature effect of metallic nanostructures. For example, the high intensity lasing may destroy the metallic nanostructures because their melting points will decrease as temperature increases. At high pump powers, the input–output curves of plasmonic lasers above the lasing threshold do not agree with the conventional laser. Also, efficient lasing device output power should be boosted to mW scale.

In summary, manipulating high-Q plasmonic resonance to enhance the performance of diverse applications have been reviewed in this section. In **Table 2**, we summarize the applications of high-Q plasmonic resonances with different resonance mechanisms. Some of these resonance mechanisms tend to specific design and application needs. For instance, SLR is suitable for plasmonic band-edge lasing; multipolar resonance is mostly used in SERS and single-photon sources; Fano resonances and GMRs are more sensitive to the change of the refractive index. Thus, understanding the principles of each resonance mechanism can guide us to design appropriate applications and achieve the desired performance.

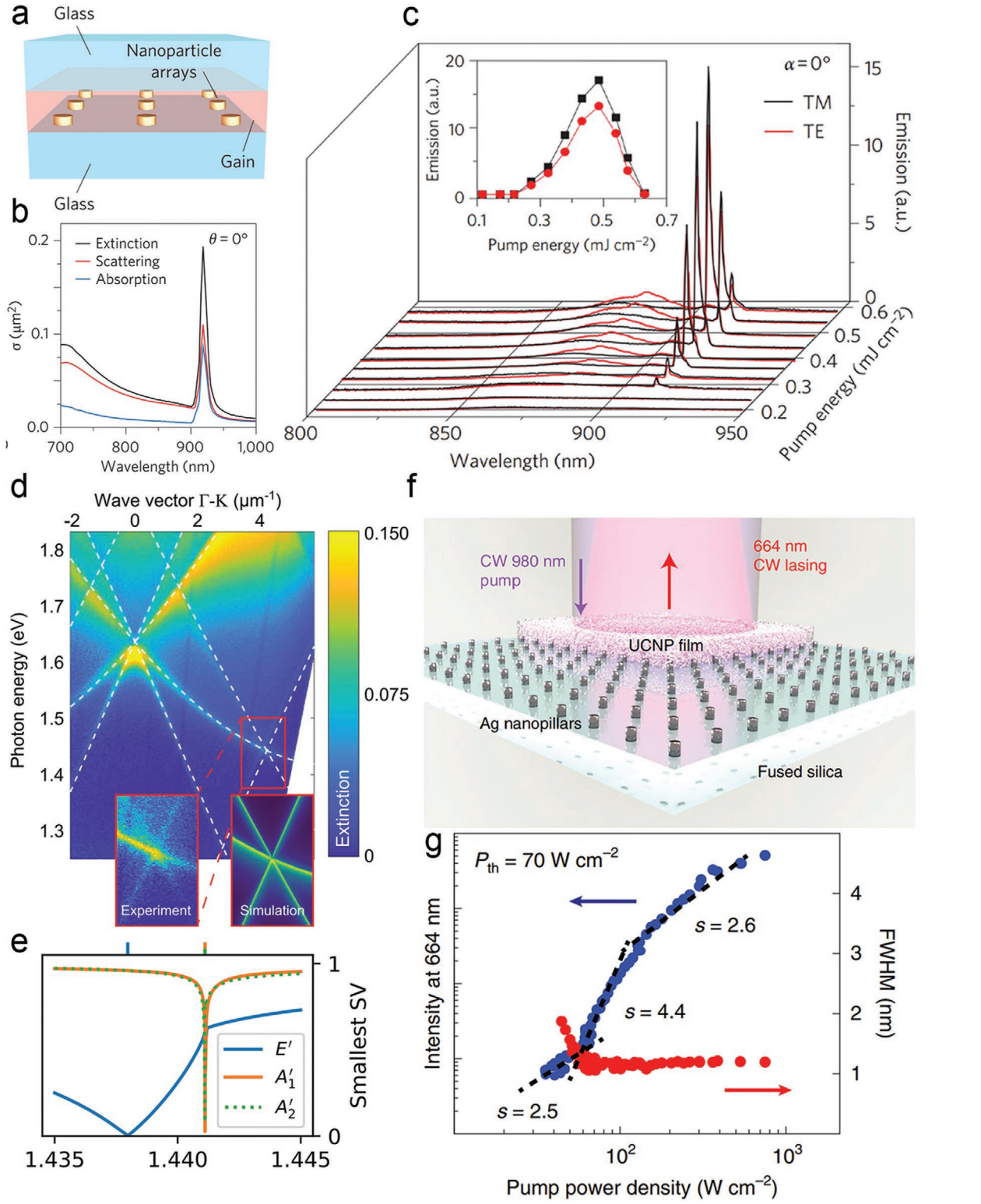

Figure 19. a) Scheme of the nanoparticle array laser. The parameter of Au nanoparticle arrays: diameter is 130 nm, height is 50 nm, and the period is 600 nm. b) Calculated extinction, scattering, and absorption spectra of 2D Au nanoparticle arrays under normal incident light. c) Measured emission spectra for different input pump pulse energies and polarizations at 800 nm pumped laser light. d) A measured angle-resolved extinction spectrum of a honeycomb lattice with particle separation of a period is 576 nm. e) The corresponding eigenmodes on the singlets and doublets obtained by group theory. f) Schematic of the upconverting nanolaser coating on top of Ag nanopillars arrays. The period of Ag arrays is 450 nm, the diameter is 80 nm, height is 50 nm. g) Input–output curves in log–log scale with emission linewidth narrowing. a–c) Reproduced with permission.[249] Copyright 2013, Springer Nature. d,e) Reproduced with permission.[254] Copyright 2019, American Physical Society. f,g) Reproduced with permission.[255] Copyright 2019, Springer Nature Limited.

Table 2. A summary of applications with different high-Q resonance mechanism.

Applications	Mechanism	FWHM [nm]	Q-factor	Performance	Ref.
Spectrally selective thermal emission	GMR	≈1000	>4	Temperature: 1000 °C	[191]
	TPP	45	88	Temperature: 150 °C	[184]
Sensors with high sensitivity	Gain-assisted plasmonic resonance	≈5	≈101	1 ppb level DNT detection	[212]
	Plasmonic Fano resonance	≈20	≈65	Sensitivity: 1277 nm RIU^{-1}; FOM*: 2.1×10^4	[203]
	SLR	20	41	Wavelength response of 6.93 nm per 1% strain variation	[202]
	GMR	0.6	1375	Sensitivity: 800 nm RIU^{-1}; FOM: 1337	[206]
Single-photon sources with boosted Purcell effect	TPP	6	109	PL enhancement factor: 2.5; Emission rate: 17 300 counts per second; $g^2(0) = 0.03$	[259]
	SLR	50	≈13	PL enhancement factor: 2.4; $g^2(0) = 0.29$	[232]
	GMR	40	≈33	Volume: $V = 2 \times 10^{-5}\ \lambda^3$; Purcell factor: $F_p = 1.68 \times 10^5$	[231]
Plasmonic filters	Plasmonic Fano resonance	79	≈21	Line width: 79 nm; transmission efficiency: 44%; polarization-insensitive	[260]
Plasmonic band-edge lasing	GMR	≈7	180	Mode volume: 0.3 $(\lambda_0/n)^3$	[261]
	SLR	≈10	≈91	Spontaneous emission rate: 200-fold enhancement; Lasing threshold: 1 mJ cm^{-2}	[249]
	SLR	4.2/6.2	197/139	Lasing threshold: 0.38 mJ cm^{-2}	[19b]
	SLR	1	664	Lasing threshold: 70 W cm^{-2}	[255]

5. Outlook and Comments

Surface plasmon has become a rapidly developing frontier interdisciplinary subject. Currently, the only practical applications of plasmonics are SERS and biosensor because the ohmic losses is not an essential factor in these applications. High-Q plasmonic resonances have essential impacts on many fields, such as energy, information, medicine, the environment, and so on. In this review, we have introduced versatile methods for generating high-Q plasmon resonances, followed by their typical applications. In addition to the several applications introduced, high-Q resonances are also essential for applications, such as switches, optical logic computing devices, hot-electron photodetection, nonlinear applications, SERS, among others.

The high-Q plasmonic resonances mean low losses in plasmonics to a large extent. Although one can design high-Q plasmonic resonance theoretically, the availability of manufacturing technology has become a technical bottleneck to the success of achieving high-Q plasmonic resonance. In the past two decades, new fabrication methods and synthesis techniques have been developed to overcome the limitation of conventional fabrication routes. However, manufacturing accuracy at nanoscale-resolution, defects, surface adsorption, etc., remain significant challenges for achieving high-Q values. The size of plasmonic particles has a pronounced effect on obtaining high-Q factors. When plasmonic particles with sizes comparable or smaller than the electron mean free path, SPR oscillations experience additional damping because of the high probability of electron collision with particle surface. Micron dimension devices have the advantages of easy fabrication, low cost, and large-scale integration, making them an ideal candidate for various targeted applications. For plasmonic applications in the visible or near-IR region, the dimensions of the devices are usually designed at nanoscale levels. As the feature size of the system reduces from micro- to nanoscale dimensions, energy losses become apparent. In the longer wavelength region, losses become manageable, and thus it is relatively easy to achieve high-Q plasmonic resonances in this area. Moreover, nanosize effects, such as lowing melting point, interface effect between metal and semiconductor heterojunctions, and oxidative properties of plasmonic materials, may further limit the usefulness of the devices in different application environments. Ultrathin metal film down to atomic thickness was predicted to possess strong plasmons and was experimentally demonstrated that it could support 2D plasmons, promising for high-Q plasmonic resonances. In general, there is a trade-off between Q-factor, fabrication practicality, and cost.

The hybrid plasmonic-dielectric system is promising for achieving high-Q resonances because it combines the advantages of both plasmonics and dielectrics. Already, strong coupling and bound states in the continuum in a hybrid plasmonic–photonic nanostructure have been observed.[256] Additionally, this strong coupling can be achieved between dark plasmon and anapole mode in a hybrid metal-dielectric system. Low-loss Luttinger liquid plasmonics in metallic single-walled carbon nanotubes are free from Landau damping, and it is worth further investigating toward achieving high-Q plasmonic resonances. Besides, instead of using the intensity of the spectrum, the polarization state-based method using plasmonic nanostructures can improve the sensing performance by using transmitted field $1/e$ spectra.

Overall, the development of high-Q plasmon resonances and their applications strongly depends on further theoretical advances and reliable fabrication of the designed structures. Although achieving high-Q plasmon resonances is challenging, it can be expected to provide solutions for next-generation photonic and optoelectronic devices. In our opinion, in the steps of putting plasmonics into practice, we should focus on

two sides. One aspect is reducing its losses; unless the metallic loss is reduced significantly, the promise of plasmonics for some applications will remain unfulfilled. Alternatively, we should consider utilizing the losses from plasmonic processes in novel designs and applications. Losses can find usefulness in photocatalysis, hot electron generation, ultrafast switching, and photothermal applications. Besides, while the losses are facing problems for the plasmonic community in the visible and near-IR region, we can focus on the midinfrared region and beyond, where the losses are manageable.

Acknowledgements

P.Y. is funded by China Postdoctoral Science Foundation (No. 2019M663467), Sichuan Science and Technology Program (No. 2020YJ0041), and National Natural Science Foundation of China (No. 62005037). The authors acknowledge the support from the National Key Research and Development Program (No. 2019YFB2203400).

Conflict of Interest

The authors declare no conflict of interest.

Keywords

high quality factors, low optical loss, narrow resonance, plasmonic resonances, resonant mechanisms

Received: September 3, 2020
Revised: December 15, 2020
Published online: January 25, 2021

[1] a) W. L. Barnes, A. Dereux, T. W. Ebbesen, *Nature* **2003**, *424*, 824; b) M. L. Brongersma, P. G. Kik, *Surface Plasmon Nanophotonics*, Springer Series in Optical Sciences, Vol. *131*, Springer, Dordrecht **2007**.
[2] a) A. V. Akimov, A. Mukherjee, C. L. Yu, D. E. Chang, A. S. Zibrov, P. R. Hemmer, H. Park, M. D. Lukin, *Nature* **2007**, *450*, 402; b) M. S. Tame, K. R. McEnery, Ş. K. Özdemir, J. Lee, S. A. Maier, M. S. Kim, *Nat. Phys.* **2013**, *9*, 329.
[3] a) M. Kauranen, A. V. Zayats, *Nat. Photonics* **2012**, *6*, 737; b) M. Mesch, B. Metzger, M. Hentschel, H. Giessen, *Nano Lett.* **2016**, *16*, 3155.
[4] a) L. Feng, P. Huo, Y. Liang, T. Xu, *Adv. Mater.* **2019**, *32*, 1903787; b) A. Sobhani, M. W. Knight, Y. Wang, B. Zheng, N. S. King, L. V. Brown, Z. Fang, P. Nordlander, N. J. Halas, *Nat. Commun.* **2013**, *4*, 1643.
[5] T. Xu, A. Agrawal, M. Abashin, K. J. Chau, H. J. Lezec, *Nature* **2013**, *497*, 470.
[6] a) K. M. Mayer, J. H. Hafner, *Chem. Rev.* **2011**, *111*, 3828; b) M. Manjappa, A. Solanki, A. Kumar, T. C. Sum, R. Singh, *Adv. Mater.* **2019**, *31*, 1901455.
[7] J.-F. Li, C.-Y. Li, R. F. Aroca, *Chem. Soc. Rev.* **2017**, *46*, 3962.
[8] a) W. Hou, S. B. Cronin, *Adv. Funct. Mater.* **2013**, *23*, 1612; b) X. Zhang, Y. L. Chen, R.-S. Liu, D. P. Tsai, *Rep. Prog. Phys.* **2013**, *76*, 046401.
[9] X. Guo, Y. Ma, Y. Wang, L. Tong, *Laser Photonics Rev.* **2013**, *7*, 855.
[10] H. A. Atwater, A. Polman, *Nat. Mater.* **2010**, *9*, 205.
[11] V. G. Kravets, A. V. Kabashin, W. L. Barnes, A. N. Grigorenko, *Chem. Rev.* **2018**, *118*, 5912.
[12] S. Kawata, *Near-Field Optics and Surface Plasmon Polaritons*, Topics in Applied Physics, Vol. *81*, Springer, Berlin **2001**.
[13] R.-M. Ma, R. F. Oulton, V. J. Sorger, X. Zhang, *Laser Photonics Rev.* **2013**, *7*, 1.
[14] S. V. Boriskina, T. A. Cooper, L. Zeng, G. Ni, J. K. Tong, Y. Tsurimaki, Y. Huang, L. Meroueh, G. Mahan, G. Chen, *Adv. Opt. Photonics* **2017**, *9*, 775.
[15] a) P. Yu, L. V. Besteiro, Y. J. Huang, J. Wu, L. Fu, H. H. Tan, C. Jagadish, G. P. Wiederrecht, A. O. Govorov, Z. M. Wang, *Adv. Opt. Mater.* **2019**, *7*, 1800995; b) J. Zou, P. Yu, W. Wang, X. Tong, L. Chang, C. Wu, W. Du, H. Ji, Y. Huang, X. Niu, A. O. Govorov, J. Wu, Z. Wang, *J. Phys. D: Appl. Phys.* **2019**, *53*, 105106.
[16] a) X. Liu, T. Tyler, T. Starr, A. F. Starr, N. M. Jokerst, W. J. Padilla, *Phys. Rev. Lett.* **2011**, *107*, 045901; b) D. G. Baranov, Y. Xiao, I. A. Nechepurenko, A. Krasnok, A. Alù, M. A. Kats, *Nat. Mater.* **2019**, *18*, 920.
[17] a) W. Wu, J. Yang, J. Zhang, J. Huang, D. Chen, H. Wang, *Opt. Lett.* **2016**, *41*, 2310; b) T. Xu, Y.-K. Wu, X. Luo, L. J. Guo, *Nat. Commun.* **2010**, *1*, 59.
[18] A. Wokaun, J. P. Gordon, P. F. Liao, *Phys. Rev. Lett.* **1982**, *48*, 957.
[19] a) C. Deeb, J.-L. Pelouard, *Phys. Chem. Chem. Phys.* **2017**, *19*, 29731; b) D. Wang, A. Yang, W. Wang, Y. Hua, R. D. Schaller, G. C. Schatz, T. W. Odom, *Nat. Nanotechnol.* **2017**, *12*, 889.
[20] Z. Liu, J. M. Steele, W. Srituravanich, Y. Pikus, C. Sun, X. Zhang, *Nano Lett.* **2005**, *5*, 1726.
[21] M. L. Juan, M. Righini, R. Quidant, *Nat. Photonics* **2011**, *5*, 349.
[22] a) K. J. Vahala, *Nature* **2003**, *424*, 839; b) L. Cong, R. Singh, *Adv. Opt. Mater.* **2019**, *7*, 1900383.
[23] a) E. Feigenbaum, M. Orenstein, *Phys. Rev. Lett.* **2008**, *101*, 163902; b) M. Kuttge, F. J. García de Abajo, A. Polman, *Nano Lett.* **2010**, *10*, 1537; c) M. Gupta, R. Singh, *Adv. Opt. Mater.* **2020**, *8*, 1902025.
[24] C. Dahmen, B. Schmidt, G. von Plessen, *Nano Lett.* **2007**, *7*, 318.
[25] P. R. West, S. Ishii, G. V. Naik, N. K. Emani, V. M. Shalaev, A. Boltasseva, *Laser Photonics Rev.* **2010**, *4*, 795.
[26] M. Bosman, L. Zhang, H. Duan, S. F. Tan, C. A. Nijhuis, C. W. Qiu, J. K. W. Yang, *Sci. Rep.* **2014**, *4*, 5537.
[27] R. F. Oulton, *Nat. Photonics* **2012**, *6*, 219.
[28] a) B. Luk'yanchuk, N. I. Zheludev, S. A. Maier, N. J. Halas, P. Nordlander, H. Giessen, C. T. Chong, *Nat. Mater.* **2010**, *9*, 707; b) V. Giannini, G. Vecchi, J. G. Rivas, *Phys. Rev. Lett.* **2010**, *105*, 266801; c) M. Kaliteevski, I. Iorsh, S. Brand, R. A. Abram, J. M. Chamberlain, A. V. Kavokin, I. A. Shelykh, *Phys. Rev. B* **2007**, *76*, 165415.
[29] B. Auguié, W. L. Barnes, *Phys. Rev. Lett.* **2008**, *101*, 143902.
[30] T. Klar, M. Perner, S. Grosse, G. Von Plessen, W. Spirkl, J. Feldmann, *Phys. Rev. Lett.* **1998**, *80*, 4249.
[31] C. Sonnichsen, T. Franzl, T. Wilk, G. von Plessen, J. Feldmann, O. Wilson, P. Mulvaney, *Phys. Rev. Lett.* **2002**, *88*, 077402.
[32] M. I. Stockman, *Opt. Express* **2011**, *19*, 22029.
[33] F. Wang, Y. R. Shen, *Phys. Rev. Lett.* **2006**, *97*, 206806.
[34] C. Ropers, D. J. Park, G. Stibenz, G. Steinmeyer, J. Kim, D. S. Kim, C. Lienau, *Phys. Rev. Lett.* **2005**, *94*, 113901.
[35] P. Zijlstra, P. M. R. Paulo, K. Yu, Q.-H. Xu, M. Orrit, *Angew. Chem.* **2012**, *51*, 8352.
[36] K. Kolwas, A. Derkachova, *J. Quant. Spectrosc. Radiat. Transfer* **2013**, *114*, 45.
[37] M. Hu, C. Novo, A. Funston, H. Wang, H. Staleva, S. Zou, P. Mulvaney, Y. Xia, G. V. Hartland, *J. Mater. Chem.* **2008**, *18*, 1949.
[38] F. Hubenthal, C. Hendrich, F. Träger, *Appl. Phys. B* **2010**, *100*, 225.
[39] M. Z. Alam, J. Meier, J. S. Aitchison, M. Mojahedi, *Opt. Express* **2007**, *15*, 176.
[40] K.-P. Chen, V. P. Drachev, J. D. Borneman, A. V. Kildishev, V. M. Shalaev, *Nano Lett.* **2010**, *10*, 916.

[41] T. G. Habteyes, S. Dhuey, E. Wood, D. Gargas, S. Cabrini, P. J. Schuck, A. P. Alivisatos, S. R. Leone, *ACS Nano* **2012**, *6*, 5702.
[42] X.-Y. Wang, Y.-L. Wang, S. Wang, B. Li, X.-W. Zhang, L. Dai, R.-M. Ma, *Nanophotonics* **2017**, *6*, 472.
[43] M. Li, S. K. Cushing, N. Wu, *Analyst* **2015**, *140*, 386.
[44] Y. Li, K. Zhao, H. Sobhani, K. Bao, P. Nordlander, *J. Phys. Chem. Lett.* **2013**, *4*, 1352.
[45] F. J. Rodríguez-Fortuño, M. Martínez-Marco, B. Tomás-Navarro, R. Ortuño, J. Martí, A. Martínez, P. J. Rodríguez-Cantó, *Appl. Phys. Lett.* **2011**, *98*, 133118.
[46] M. W. Knight, Y. Wu, J. B. Lassiter, P. Nordlander, N. J. Halas, *Nano Lett.* **2009**, *9*, 2188.
[47] A. Sobhani, A. Manjavacas, Y. Cao, M. J. McClain, F. J. García de Abajo, P. Nordlander, N. J. Halas, *Nano Lett.* **2015**, *15*, 6946.
[48] a) M.-K. Kim, S. H. Lee, M. Choi, B.-H. Ahn, N. Park, Y.-H. Lee, B. Min, *Opt. Express* **2010**, *18*, 11089; b) Z. Tian, R. Singh, J. Han, J. Gu, Q. Xing, J. Wu, W. Zhang, *Opt. Lett.* **2010**, *35*, 3586.
[49] L. Y. M. Tobing, G.-Y. Goh, A. D. Mueller, L. Ke, Y. Luo, D.-H. Zhang, *Sci. Rep.* **2017**, *7*, 7539.
[50] T. Zentgraf, S. Zhang, R. F. Oulton, X. Zhang, *Phys. Rev. B* **2009**, *80*, 195415.
[51] R.-M. Ma, R. F. Oulton, V. J. Sorger, G. Bartal, X. Zhang, *Nat. Mater.* **2011**, *10*, 110.
[52] C. Cherqui, M. R. Bourgeois, D. Wang, G. C. Schatz, *Acc. Chem. Res.* **2019**, *52*, 2548.
[53] W. Cao, R. Singh, I. A. I. Al-Naib, M. He, A. J. Taylor, W. Zhang, *Opt. Lett.* **2012**, *37*, 3366.
[54] S. Zhang, D. A. Genov, Y. Wang, M. Liu, X. Zhang, *Phys. Rev. Lett.* **2008**, *101*, 047401.
[55] X. Yu, L. Shi, D. Han, J. Zi, P. V. Braun, *Adv. Funct. Mater.* **2010**, *20*, 1910.
[56] Z.-Y. Yang, S. Ishii, T. Yokoyama, T. D. Dao, M.-G. Sun, P. S. Pankin, I. V. Timofeev, T. Nagao, K.-P. Chen, *ACS Photonics* **2017**, *4*, 2212.
[57] a) P. Ding, G. Cai, J. Wang, J. He, C. Fan, X. Liu, E. Liang, *J. Opt.* **2014**, *16*, 065003; b) C. L. Haynes, A. D. McFarland, L. Zhao, R. P. Van Duyne, G. C. Schatz, L. Gunnarsson, J. Prikulis, B. Kasemo, M. Käll, *J. Phys. Chem. B* **2003**, *107*, 7337; c) T. S. A. Safiabadi, Z. Wei, *Nanophotonics* **2019**, *8*, 1199.
[58] D. Wang, J. Guan, J. Hu, M. R. Bourgeois, T. W. Odom, *Acc. Chem. Res.* **2019**, *52*, 2997.
[59] a) L. Zhao, K. L. Kelly, G. C. Schatz, *J. Phys. Chem. B* **2003**, *107*, 7343; b) S. Zou, N. Janel, G. C. Schatz, *J. Chem. Phys.* **2004**, *120*, 10871.
[60] V. G. Kravets, F. Schedin, A. N. Grigorenko, *Phys. Rev. Lett.* **2008**, *101*, 087403.
[61] X. Yang, G. Xiao, Y. Lu, G. Li, *Opt. Express* **2019**, *27*, 25384.
[62] A. D. Humphrey, N. Meinzer, T. A. Starkey, W. L. Barnes, *ACS Photonics* **2016**, *3*, 634.
[63] A. D. Humphrey, W. L. Barnes, *Phys. Rev. B* **2014**, *90*, 075404.
[64] S. R. K. Rodriguez, M. C. Schaafsma, A. Berrier, J. Gómez Rivas, *Physica B* **2012**, *407*, 4081.
[65] Q. Le-Van, E. Zoethout, E.-J. Geluk, M. Ramezani, M. Berghuis, J. G. Rivas, *Adv. Opt. Mater.* **2019**, *7*, 1801451.
[66] B. Auguié, W. L. Barnes, *Opt. Lett.* **2009**, *34*, 401.
[67] B. Auguié, X. M. Bendaña, W. L. Barnes, F. J. García de Abajo, *Phys. Rev. B* **2010**, *82*, 155447.
[68] S.-Q. Li, W. Zhou, D. B. Buchholz, J. B. Ketterson, L. E. Ocola, K. Sakoda, R. P. H. Chang, *Appl. Phys. Lett.* **2014**, *104*, 231101.
[69] W. Zhou, T. W. Odom, *Nat. Nanotechnol.* **2011**, *6*, 423.
[70] Y. Xiuhua, X. Lei, L. Yuanfu, L. Guangyuan, *J. Phys. D: Appl. Phys.* **2020**, *53*, 465109.
[71] J. Henzie, M. H. Lee, T. W. Odom, *Nat. Nanotechnol.* **2007**, *2*, 549.
[72] D. Wang, A. Yang, A. J. Hryn, G. C. Schatz, T. W. Odom, *ACS Photonics* **2015**, *2*, 1789.
[73] a) S. Baur, S. Sanders, A. Manjavacas, *ACS Nano* **2018**, *12*, 1618; b) R. Li, M. R. Bourgeois, C. Cherqui, J. Guan, D. Wang, J. Hu, R. D. Schaller, G. C. Schatz, T. W. Odom, *Nano Lett.* **2019**, *19*, 6435.
[74] N. J. Halas, S. Lal, W.-S. Chang, S. Link, P. Nordlander, *Chem. Rev.* **2011**, *111*, 3913.
[75] Z. Li, S. Butun, K. Aydin, *ACS Nano* **2014**, *8*, 8242.
[76] K. Sakai, K. Nomura, T. Yamamoto, T. Omura, K. Sasaki, *Sci. Rep.* **2016**, *6*, 34967.
[77] X. Zhu, G. M. Imran Hossain, M. George, A. Farhang, A. Cicek, A. A. Yanik, *ACS Photonics* **2020**, *7*, 416.
[78] S. Thongrattanasiri, F. J. García de Abajo, *Phys. Rev. Lett.* **2013**, *110*, 187401.
[79] A. Yang, A. J. Hryn, M. R. Bourgeois, W.-K. Lee, J. Hu, G. C. Schatz, T. W. Odom, *Proc. Natl. Acad. Sci. USA* **2016**, *113*, 14201.
[80] V. I. Zakomirnyi, I. L. Rasskazov, V. S. Gerasimov, A. E. Ershov, S. P. Polyutov, S. V. Karpov, *Appl. Phys. Lett.* **2017**, *111*, 123107.
[81] N. G. Bastús, J. Piella, V. Puntes, *Langmuir* **2016**, *32*, 290.
[82] X. Zambrana-Puyalto, X. Vidal, G. Molina-Terriza, *Opt. Express* **2012**, *20*, 24536.
[83] E. E. Radescu, G. Vaman, *Phys. Rev. E* **2002**, *65*, 046609.
[84] M.-W. Chu, V. Myroshnychenko, C. H. Chen, J.-P. Deng, C.-Y. Mou, F. J. García de Abajo, *Nano Lett.* **2009**, *9*, 399.
[85] D. Rossouw, M. Couillard, J. Vickery, E. Kumacheva, G. A. Botton, *Nano Lett.* **2011**, *11*, 1499.
[86] N. M. Mojarad, M. Agio, *Opt. Express* **2009**, *17*, 117.
[87] M. Liu, T.-W. Lee, S. K. Gray, P. Guyot-Sionnest, M. Pelton, *Phys. Rev. Lett.* **2009**, *102*, 107401.
[88] E.-A. You, W. Zhou, J. Y. Suh, M. D. Huntington, T. W. Odom, *ACS Nano* **2012**, *6*, 1786.
[89] E. Kazuma, T. Tatsuma, *J. Phys. Chem. C* **2013**, *117*, 2435.
[90] K. L. Kelly, E. Coronado, L. L. Zhao, G. C. Schatz, *J. Phys. Chem. B* **2003**, *107*, 668.
[91] H. Liang, D. Rossouw, H. Zhao, S. K. Cushing, H. Shi, A. Korinek, H. Xu, F. Rosei, W. Wang, N. Wu, G. A. Botton, D. Ma, *J. Am. Chem. Soc.* **2013**, *135*, 9616.
[92] a) S. D. Liu, Z. S. Zhang, Q. Q. Wang, *Opt. Express* **2009**, *17*, 2906; b) W. Wang, P. Yu, Z. Zhong, X. Tong, T. Liu, Y. Li, E. Ashalley, H. Chen, J. Wu, Z. Wang, *Nanotechnology* **2018**, *29*, 355402.
[93] G. Dayal, S. Anantha Ramakrishna, *J. Opt.* **2014**, *16*, 094016.
[94] H. Wei, A. Reyes-Coronado, P. Nordlander, J. Aizpurua, H. Xu, *ACS Nano* **2010**, *4*, 2649.
[95] S. Zhang, L. Chen, Y. Huang, H. Xu, *Nanoscale* **2013**, *5*, 6985.
[96] J. Martin, M. Kociak, Z. Mahfoud, J. Proust, D. Gérard, J. Plain, *Nano Lett.* **2014**, *14*, 5517.
[97] N. Hooshmand, M. A. El-Sayed, *Proc. Natl. Acad. Sci. USA* **2019**, *116*, 19299.
[98] S.-D. Liu, Z. Yang, R.-P. Liu, X.-Y. Li, *Appl. Phys. Lett.* **2012**, *100*, 203119.
[99] L. Y. M. Tobing, D.-H. Zhang, *Adv. Mater.* **2016**, *28*, 889.
[100] Y. Francescato, V. Giannini, S. A. Maier, *ACS Nano* **2012**, *6*, 1830.
[101] J. Chen, F. Gan, Y. Wang, G. Li, *Adv. Opt. Mater.* **2018**, *6*, 1701152.
[102] a) U. Fano, *Phys. Rev.* **1961**, *124*, 1866; b) J. Sancho-Parramon, S. Bosch, *ACS Nano* **2012**, *6*, 8415; c) M. Gupta, R. Singh, *Adv. Opt. Mater.* **2016**, *4*, 2119.
[103] S. Zhang, K. Bao, N. J. Halas, H. Xu, P. Nordlander, *Nano Lett.* **2011**, *11*, 1657.
[104] T. C. W. Tan, E. Plum, R. Singh, *Adv. Opt. Mater.* **2020**, *8*, 1901572.
[105] a) N. A. Mirin, K. Bao, P. Nordlander, *J. Phys. Chem. A* **2009**, *113*, 4028; b) I. Al-Naib, Y. Yang, M. M. Dignam, W. Zhang, R. Singh, *Appl. Phys. Lett.* **2015**, *106*, 011102.
[106] J. Chen, Z. Li, Y. Zou, Z. Deng, J. Xiao, Q. Gong, *Plasmonics* **2013**, *8*, 1627.
[107] W. X. Lim, M. Manjappa, P. Pitchappa, R. Singh, *Adv. Opt. Mater.* **2018**, *6*, 1800502.

[108] Y. H. Fu, J. B. Zhang, Y. F. Yu, B. Luk'yanchuk, *ACS Nano* **2012**, *6*, 5130.
[109] J. Wang, C. Fan, J. He, P. Ding, E. Liang, Q. Xue, *Opt. Express* **2013**, *21*, 2236.
[110] R. Zafar, M. Salim, *IEEE Sens. J.* **2015**, *15*, 6313.
[111] M. Zhang, J. Fang, F. Zhang, J. Chen, H. Yu, *Opt. Commun.* **2017**, *405*, 216.
[112] S. Li, Y. Zhang, X. Song, Y. Wang, L. Yu, *Opt. Express* **2016**, *24*, 15351.
[113] K.-L. Lee, J.-B. Huang, J.-W. Chang, S.-H. Wu, P.-K. Wei, *Sci. Rep.* **2015**, *5*, 8547.
[114] Y. K. Srivastava, M. Manjappa, H. N. S. Krishnamoorthy, R. Singh, *Adv. Opt. Mater.* **2016**, *4*, 1875.
[115] A. E. Miroshnichenko, *Phys. Rev. E* **2009**, *79*, 026611.
[116] V. Krivenkov, S. Goncharov, I. Nabiev, Y. P. Rakovich, *Laser Photonics Rev.* **2019**, *13*, 1800176.
[117] C. L. Garrido Alzar, M. A. G. Martinez, P. Nussenzveig, *Am. J. Phys.* **2001**, *70*, 37.
[118] S. Paul, M. Ray, *Plasmonics* **2019**, *14*, 1113.
[119] Z. Han, S. I. Bozhevolnyi, *Opt. Express* **2011**, *19*, 3251.
[120] N. Liu, L. Langguth, T. Weiss, J. Kästel, M. Fleischhauer, T. Pfau, H. Giessen, *Nat. Mater.* **2009**, *8*, 758.
[121] C.-Y. Chen, I.-W. Un, N.-H. Tai, T.-J. Yen, *Opt. Express* **2009**, *17*, 15372.
[122] J. Wang, B. Yuan, C. Fan, J. He, P. Ding, Q. Xue, E. Liang, *Opt. Express* **2013**, *21*, 25159.
[123] J. He, P. Ding, J. Wang, C. Fan, E. Liang, *Opt. Express* **2015**, *23*, 6083.
[124] Z. Vafapour, H. Alaei, *Plasmonics* **2017**, *12*, 479.
[125] X. He, X. Yang, G. Lu, W. Yang, F. Wu, Z. Yu, J. Jiang, *Carbon* **2017**, *123*, 668.
[126] C. Zeng, Y. Cui, X. Liu, *Opt. Express* **2015**, *23*, 545.
[127] Z. Li, Y. Ma, R. Huang, R. Singh, J. Gu, Z. Tian, J. Han, W. Zhang, *Opt. Express* **2011**, *19*, 8912.
[128] J. Gu, R. Singh, X. Liu, X. Zhang, Y. Ma, S. Zhang, S. A. Maier, Z. Tian, A. K. Azad, H.-T. Chen, A. J. Taylor, J. Han, W. Zhang, *Nat. Commun.* **2012**, *3*, 1151.
[129] O. Limaj, F. Giorgianni, A. Di Gaspare, V. Giliberti, G. de Marzi, P. Roy, M. Ortolani, X. Xi, D. Cunnane, S. Lupi, *ACS Photonics* **2014**, *1*, 570.
[130] Y. He, H. Zhou, Y. Jin, S. He, *Appl. Phys. Lett.* **2011**, *99*, 043113.
[131] H. Lu, X. Liu, D. Mao, Y. Gong, G. Wang, *Opt. Lett.* **2011**, *36*, 3233.
[132] T. Wang, Y. Zhang, Z. Hong, Z. Han, *Opt. Express* **2014**, *22*, 21529.
[133] J. Chen, C. Wang, R. Zhang, J. Xiao, *Opt. Lett.* **2012**, *37*, 5133.
[134] Z. Chen, H. Li, S. Zhan, B. Li, Z. He, H. Xu, M. Zheng, *Sci. Rep.* **2016**, *6*, 24446.
[135] X. Wu, S. K. Gray, M. Pelton, *Opt. Express* **2010**, *18*, 23633.
[136] H. Lu, X. Gan, D. Mao, B. Jia, J. Zhao, *Sci. Rep.* **2018**, *8*, 1558.
[137] H. Choo, M.-K. Kim, M. Staffaroni, T. J. Seok, J. Bokor, S. Cabrini, P. J. Schuck, M. C. Wu, E. Yablonovitch, *Nat. Photonics* **2012**, *6*, 838.
[138] X. Lu, R. Wan, T. Zhang, *Opt. Express* **2015**, *23*, 29842.
[139] J. A. Porto, F. J. García-Vidal, J. B. Pendry, *Phys. Rev. Lett.* **1999**, *83*, 2845.
[140] S. J. P. Kress, F. V. Antolinez, P. Richner, S. V. Jayanti, D. K. Kim, F. Prins, A. Riedinger, M. P. C. Fischer, S. Meyer, K. M. McPeak, D. Poulikakos, D. J. Norris, *Nano Lett.* **2015**, *15*, 6267.
[141] a) S. Zhang, C. Gu, H. Xu, *Small* **2014**, *10*, 4264; b) H. Wei, D. Pan, S. Zhang, Z. Li, Q. Li, N. Liu, W. Wang, H. Xu, *Chem. Rev.* **2018**, *118*, 2882.
[142] C. L. C. Smith, N. Stenger, A. Kristensen, N. A. Mortensen, S. I. Bozhevolnyi, *Nanoscale* **2015**, *7*, 9355.
[143] S. Linden, J. Kuhl, H. Giessen, *Phys. Rev. Lett.* **2001**, *86*, 4688.
[144] Y. Fang, M. Sun, *Light Sci. Appl.* **2015**, *4*, e294.
[145] V. J. Sorger, R. F. Oulton, J. Yao, G. Bartal, X. Zhang, *Nano Lett.* **2009**, *9*, 3489.
[146] R. Ameling, L. Langguth, M. Hentschel, M. Mesch, P. V. Braun, H. Giessen, *Appl. Phys. Lett.* **2010**, *97*, 253116.
[147] W. Zhu, T. Xu, H. Wang, C. Zhang, P. B. Deotare, A. Agrawal, H. J. Lezec, *Sci. Adv.* **2017**, *3*, e1700909.
[148] D. Chanda, K. Shigeta, T. Truong, E. Lui, A. Mihi, M. Schulmerich, P. V. Braun, R. Bhargava, J. A. Rogers, *Nat. Commun.* **2011**, *2*, 479.
[149] S. Luo, J. Zhao, D. Zuo, X. Wang, *Opt. Express* **2016**, *24*, 9288.
[150] D. Wu, R. Li, Y. Liu, Z. Yu, L. Yu, L. Chen, C. Liu, R. Ma, H. Ye, *Nanoscale Res. Lett.* **2017**, *12*, 427.
[151] B. Fix, J. Jaeck, P. Bouchon, S. Héron, B. Vest, R. Haïdar, *Opt. Lett.* **2017**, *42*, 5062.
[152] R. Thijssen, E. Verhagen, T. J. Kippenberg, A. Polman, *Nano Lett.* **2013**, *13*, 3293.
[153] R. F. Oulton, V. J. Sorger, D. A. Genov, D. F. P. Pile, X. Zhang, *Nat. Photonics* **2008**, *2*, 496.
[154] X. Liu, J. Gao, J. Gao, H. Yang, X. Wang, T. Wang, Z. Shen, Z. Liu, H. Liu, J. Zhang, Z. Li, Y. Wang, Q. Li, *Light Sci. Appl.* **2018**, *7*, 14.
[155] S. Sarkar, V. Gupta, M. Kumar, J. Schubert, P. T. Probst, J. Joseph, T. A. F. König, *ACS Appl. Mater. Interfaces* **2019**, *11*, 13752.
[156] L. He, Ş. K. Özdemir, L. Yang, *Laser Photonics Rev.* **2013**, *7*, 60.
[157] B. Min, E. Ostby, V. Sorger, E. Ulin-Avila, L. Yang, X. Zhang, K. Vahala, *Nature* **2009**, *457*, 455.
[158] Y. F. Xiao, C. L. Zou, B. B. Li, Y. Li, C. H. Dong, Z. F. Han, Q. Gong, *Phys. Rev. Lett.* **2010**, *105*, 153902.
[159] G. Dayal, X. Y. Chin, C. Soci, R. Singh, *Adv. Opt. Mater.* **2016**, *4*, 1295.
[160] Y. Su, P. Chang, C. Lin, A. S. Helmy, *Sci. Adv.* **2019**, *5*, eaav1790.
[161] a) W. Gao, J. Shu, C. Qiu, Q. Xu, *ACS Nano* **2012**, *6*, 7806; b) J. R. Piper, S. Fan, *ACS Photonics* **2014**, *1*, 347; c) Y. Long, Y. Li, L. Shen, W. Liang, H. Deng, H. Xu, *J. Phys. D: Appl. Phys.* 415103, **2016**, *49*; d) Y.-L. Liao, Y. Zhao, *Opt. Express* **2017**, *25*, 32080.
[162] M. E. Sasin, R. P. Seisyan, M. A. Kalitteevski, S. Brand, R. A. Abram, J. M. Chamberlain, A. Y. Egorov, A. P. Vasil'ev, V. S. Mikhrin, A. V. Kavokin, *Appl. Phys. Lett.* **2008**, *92*, 251112.
[163] A. Kumari, S. Kumar, M. K. Shukla, G. Kumar, P. S. Maji, R. Vijaya, R. Das, *J. Phys. D: Appl. Phys.* **2018**, *51*, 255103.
[164] C. Grossmann, C. Coulson, G. Christmann, I. Farrer, H. E. Beere, D. A. Ritchie, J. J. Baumberg, *Appl. Phys. Lett.* **2011**, *98*, 231105.
[165] B. I. Afinogenov, V. O. Bessonov, A. A. Nikulin, A. A. Fedyanin, *Appl. Phys. Lett.* **2013**, *103*, 061112.
[166] H. Y. Dong, J. Wang, T. J. Cui, *Phys. Rev. B* **2013**, *87*, 045406.
[167] G. R. Bikbaev, Y. S. Vetrov, V. I. Timofeev, *Photonics* **2019**, *6*, 28.
[168] H. Zhu, H. Luo, Q. Li, D. Zhao, L. Cai, K. Du, Z. Xu, P. Ghosh, M. Qiu, *Opt. Lett.* **2018**, *43*, 5230.
[169] H. Lu, Y. Li, H. Jiao, Z. Li, D. Mao, J. Zhao, *Opt. Express* **2019**, *27*, 5383.
[170] N. Lundt, S. Klembt, E. Cherotchenko, S. Betzold, O. Iff, A. V. Nalitov, M. Klaas, C. P. Dietrich, A. V. Kavokin, S. Höfling, C. Schneider, *Nat. Commun.* **2016**, *7*, 13328.
[171] M. Wurdack, N. Lundt, M. Klaas, V. Baumann, A. V. Kavokin, S. Höfling, C. Schneider, *Nat. Commun.* **2017**, *8*, 259.
[172] H. Lu, X. Gan, B. Jia, D. Mao, J. Zhao, *Opt. Lett.* **2016**, *41*, 4743.
[173] C. Zhang, K. Wu, V. Giannini, X. Li, *ACS Nano* **2017**, *11*, 1719.
[174] C. Symonds, G. Lheureux, J. P. Hugonin, J. J. Greffet, J. Laverdant, G. Brucoli, A. Lemaitre, P. Senellart, J. Bellessa, *Nano Lett.* **2013**, *13*, 3179.
[175] T. Asano, K. Mochizuki, M. Yamaguchi, M. Chaminda, S. Noda, *Opt. Express* **2009**, *17*, 19190.
[176] J. J. Talghader, A. S. Gawarikar, R. P. Shea, *Light Sci. Appl.* **2012**, *1*, e24.
[177] R. Sakakibara, V. Stelmakh, W. R. Chan, M. Ghebrebrhan, J. D. Joannopoulos, M. Soljacic, I. Čelanović, *J. Photonics Energy* **2019**, *9*, 1.

[178] K. Cui, P. Lemaire, H. Zhao, T. Savas, G. Parsons, A. J. Hart, *Adv. Energy Mater.* **2018**, *8*, 1801471.
[179] I. El-Kady, R. Biswas, Y. Ye, M. F. Su, I. Puscasu, M. Pralle, E. A. Johnson, J. Daly, A. Greenwald, *Photonics Nanostruct.: Fundam. Appl.* **2003**, *1*, 69.
[180] M.-W. Tsai, T.-H. Chuang, C.-Y. Meng, Y.-T. Chang, S.-C. Lee, *Appl. Phys. Lett.* **2006**, *89*, 173116.
[181] M. N. Abbas, C.-W. Cheng, Y.-C. Chang, M.-H. Shih, H.-H. Chen, S.-C. Lee, *Appl. Phys. Lett.* **2011**, *98*, 121116.
[182] A. Kazemi Moridani, R. Zando, W. Xie, I. Howell, J. J. Watkins, J.-H. Lee, *Adv. Opt. Mater.* **2017**, *5*, 1600993.
[183] Z. Wang, J. K. Clark, L.-C. Huang, Y.-L. Ho, J.-J. Delaunay, *Appl. Phys. Lett.* **2017**, *110*, 251102.
[184] Z. Wang, J. K. Clark, Y.-L. Ho, B. Vilquin, H. Daiguji, J.-J. Delaunay, *ACS Photonics* **2018**, *5*, 2446.
[185] J. A. Mason, D. C. Adams, Z. Johnson, S. Smith, A. W. Davis, D. Wasserman, *Opt. Express* **2010**, *18*, 25192.
[186] T. D. Dao, K. Chen, S. Ishii, A. Ohi, T. Nabatame, M. Kitajima, T. Nagao, *ACS Photonics* **2015**, *2*, 964.
[187] U. Guler, A. Boltasseva, V. M. Shalaev, *Science* **2014**, *344*, 263.
[188] S. Tay, A. Kropachev, I. E. Araci, T. Skotheim, R. A. Norwood, N. Peyghambarian, *Appl. Phys. Lett.* **2009**, *94*, 071113.
[189] H. Wang, Q. Chen, L. Wen, S. Song, X. Hu, G. Xu, *Photonics Res.* **2015**, *3*, 329.
[190] D. Jiang, W. Yang, *Sol. Energy Mater. Sol. Cells* **2017**, *163*, 98.
[191] T. Yokoyama, T. D. Dao, K. Chen, S. Ishii, R. P. Sugavaneshwar, M. Kitajima, T. Nagao, *Adv. Opt. Mater.* **2016**, *4*, 1987.
[192] B. Zhao, L. Wang, Y. Shuai, Z. M. Zhang, *Int. J. Heat Mass Transfer* **2013**, *67*, 637.
[193] Z.-y. Yang, S. Ishii, T. Yokoyama, T. D. Dao, M.-g. Sun, T. Nagao, K.-p. Chen, *Opt. Lett.* **2016**, *41*, 4453.
[194] E. Rephaeli, S. Fan, *Opt. Express* **2009**, *17*, 15145.
[195] D. Chubb, *Fundamentals of Thermophotovoltaic Energy Conversion*, Elsevier, Amsterdam **2007**.
[196] P. Nagpal, S. E. Han, A. Stein, D. J. Norris, *Nano Lett.* **2008**, *8*, 3238.
[197] E. Sakr, P. Bermel, *Opt. Express* **2017**, *25*, A880.
[198] D. Woolf, J. Hensley, J. G. Cederberg, D. T. Bethke, A. D. Grine, E. A. Shaner, *Appl. Phys. Lett.* **2014**, *105*, 081110.
[199] C. Ng, L. Wesemann, E. Panchenko, J. Song, T. J. Davis, A. Roberts, D. E. Gómez, *Adv. Opt. Mater.* **2019**, *7*, 1801660.
[200] N. Liu, M. Mesch, T. Weiss, M. Hentschel, H. Giessen, *Nano Lett.* **2010**, *10*, 2342.
[201] Y. H. Lee, H. Chen, Q.-H. Xu, J. Wang, *J. Phys. Chem. C* **2011**, *115*, 7997.
[202] K.-H. Chang, J.-S. Cheng, T.-W. Lu, P.-T. Lee, *Opt. Express* **2018**, *26*, 33215.
[203] Y. Binfeng, Z. Ruohu, H. Guohua, C. Yiping, *Plasmonics* **2016**, *11*, 1157.
[204] L. Meng, D. Zhao, Y. Yang, F. J. García de Abajo, Q. Li, Z. Ruan, M. Qiu, *Phys. Rev. Appl.* **2019**, *11*, 044030.
[205] A. A. Rifat, G. A. Mahdiraji, Y. M. Sua, R. Ahmed, Y. G. Shee, F. R. M. Adikan, *Opt. Express* **2016**, *24*, 2485.
[206] Z. Liu, G. Liu, X. Liu, G. Fu, *Nanotechnology* **2019**, *31*, 115208.
[207] B. Liu, S. Chen, J. Zhang, X. Yao, J. Zhong, H. Lin, T. Huang, Z. Yang, J. Zhu, S. Liu, C. Lienau, L. Wang, B. Ren, *Adv. Mater.* **2018**, *30*, 1706031.
[208] W. Chen, S. Zhang, Q. Deng, H. Xu, *Nat. Commun.* **2018**, *9*, 801.
[209] A. Tittl, P. Mai, R. Taubert, D. Dregely, N. Liu, H. Giessen, *Nano Lett.* **2011**, *11*, 4366.
[210] A. A. Yanik, A. E. Cetin, M. Huang, A. Artar, S. H. Mousavi, A. Khanikaev, J. H. Connor, G. Shvets, H. Altug, *Proc. Natl. Acad. Sci. USA* **2011**, *108*, 11784.
[211] K. Chen, R. Adato, H. Altug, *ACS Nano* **2012**, *6*, 7998.
[212] R.-M. Ma, S. Ota, Y. Li, S. Yang, X. Zhang, *Nat. Nanotechnol.* **2014**, *9*, 600.
[213] A. Kristensen, J. K. W. Yang, S. I. Bozhevolnyi, S. Link, P. Nordlander, N. J. Halas, N. A. Mortensen, *Nat. Rev. Mater.* **2016**, *2*, 16088.
[214] J. R. Mejía-Salazar, O. N. Oliveira, *Chem. Rev.* **2018**, *118*, 10617.
[215] P. Yu, Z. Li, T. Wu, Y.-T. Wang, X. Tong, C.-F. Li, Z. Wang, S.-H. Wei, Y. Zhang, H. Liu, L. Fu, Y. Zhang, J. Wu, H. H. Tan, C. Jagadish, Z. M. Wang, *ACS Nano* **2019**, *13*, 13492.
[216] M. D. Eisaman, J. Fan, A. Migdall, S. V. Polyakov, *Rev. Sci. Instrum.* **2011**, *82*, 071101.
[217] F. Liu, A. J. Brash, J. O'Hara, L. M. P. P. Martins, C. L. Phillips, R. J. Coles, B. Royall, E. Clarke, C. Bentham, N. Prtljaga, I. E. Itskevich, L. R. Wilson, M. S. Skolnick, A. M. Fox, *Nat. Nanotechnol.* **2018**, *13*, 835.
[218] P. Lalanne, S. Mias, J. P. Hugonin, *Opt. Express* **2004**, *12*, 458.
[219] A. F. Koenderink, *Nano Lett.* **2009**, *9*, 4228.
[220] A. G. Curto, G. Volpe, T. H. Taminiau, M. P. Kreuzer, R. Quidant, N. F. van Hulst, *Science* **2010**, *329*, 930.
[221] S. Schietinger, M. Barth, T. Aichele, O. Benson, *Nano Lett.* **2009**, *9*, 1694.
[222] V. Caligiuri, M. Palei, M. Imran, L. Manna, R. Krahne, *ACS Photonics* **2018**, *5*, 2287.
[223] J. T. Choy, B. J. M. Hausmann, T. M. Babinec, I. Bulu, M. Khan, P. Maletinsky, A. Yacoby, M. Lončar, *Nat. Photonics* **2011**, *5*, 738.
[224] L. Y. M. Tobing, D. H. Zhang, K. E. Fong, M. D. Birowosuto, Y. Gao, C. Dang, H. V. Demir, *ACS Photonics* **2018**, *5*, 1566.
[225] C.-H. Cho, C. O. Aspetti, M. E. Turk, J. M. Kikkawa, S.-W. Nam, R. Agarwal, *Nat. Mater.* **2011**, *10*, 669.
[226] H. M. Doeleman, E. Verhagen, A. F. Koenderink, *ACS Photonics* **2016**, *3*, 1943.
[227] K. J. Russell, T.-L. Liu, S. Cui, E. L. Hu, *Nat. Photonics* **2012**, *6*, 459.
[228] E. J. R. Vesseur, F. J. G. de Abajo, A. Polman, *Phys. Rev. B* **2010**, *82*, 165419.
[229] G. M. Akselrod, C. Argyropoulos, T. B. Hoang, C. Ciracì, C. Fang, J. Huang, D. R. Smith, M. H. Mikkelsen, *Nat. Photonics* **2014**, *8*, 835.
[230] Y. Luo, E. D. Ahmadi, K. Shayan, Y. Ma, K. S. Mistry, C. Zhang, J. Hone, J. L. Blackburn, S. Strauf, *Nat. Commun.* **2017**, *8*, 1413.
[231] G. Zhang, S. Jia, Y. Gu, J. Chen, *Laser Photonics Rev.* **2019**, *13*, 1900025.
[232] T. T. Tran, D. Wang, Z.-Q. Xu, A. Yang, M. Toth, T. W. Odom, I. Aharonovich, *Nano Lett.* **2017**, *17*, 2634.
[233] O. Gazzano, S. Michaelis de Vasconcellos, K. Gauthron, C. Symonds, P. Voisin, J. Bellessa, A. Lemaître, P. Senellart, *Appl. Phys. Lett.* **2012**, *100*, 232111.
[234] A. Tamada, Y. Ota, K. Kuruma, K. Watanabe, S. Iwamoto, Y. Arakawa, *ACS Photonics* **2019**, *6*, 1106.
[235] P. Senellart, G. Solomon, A. White, *Nat. Nanotechnol.* **2017**, *12*, 1026.
[236] a) Y. S. Do, J. H. Park, B. Y. Hwang, S.-M. Lee, B.-K. Ju, K. C. Choi, *Adv. Opt. Mater.* **2013**, *1*, 133; b) Q. Chen, X. Hu, L. Wen, Y. Yu, D. R. S. Cumming, *Small* **2016**, *12*, 4922.
[237] I. J. H. McCrindle, J. Grant, T. D. Drysdale, D. R. S. Cumming, *Adv. Opt. Mater.* **2014**, *2*, 149.
[238] A. Miyamichi, A. Ono, H. Kamehama, K. Kagawa, K. Yasutomi, S. Kawahito, *Opt. Express* **2018**, *26*, 25178.
[239] D. Fleischman, K. T. Fountaine, C. R. Bukowsky, G. Tagliabue, L. A. Sweatlock, H. A. Atwater, *ACS Photonics* **2019**, *6*, 332.
[240] S. Yokogawa, S. P. Burgos, H. A. Atwater, *Nano Lett.* **2012**, *12*, 4349.
[241] X. Luo, X. Zou, X. Li, Z. Zhou, W. Pan, L. Yan, K. Wen, *Opt. Lett.* **2013**, *38*, 1585.

[242] S. Khani, M. Danaie, P. Rezaei, *Plasmonics* **2019**, *14*, 53.
[243] W. Lai, K. Wen, J. Lin, Z. Guo, Q. Hu, Y. Fang, *Appl. Opt.* **2018**, *57*, 6369.
[244] Z. Li, A. W. Clark, J. M. Cooper, *ACS Nano* **2016**, *10*, 492.
[245] H. Altug, D. Englund, J. Vučković, *Nat. Phys.* **2006**, *2*, 484.
[246] F. van Beijnum, P. J. van Veldhoven, E. J. Geluk, M. J. A. de Dood, G. W. 't Hooft, M. P. van Exter, *Phys. Rev. Lett.* **2013**, *110*, 206802.
[247] A. H. Schokker, A. F. Koenderink, *Phys. Rev. B* **2014**, *90*, 155452.
[248] J. Y. Suh, C. H. Kim, W. Zhou, M. D. Huntington, D. T. Co, M. R. Wasielewski, T. W. Odom, *Nano Lett.* **2012**, *12*, 5769.
[249] W. Zhou, M. Dridi, J. Y. Suh, C. H. Kim, D. T. Co, M. R. Wasielewski, G. C. Schatz, T. W. Odom, *Nat. Nanotechnol.* **2013**, *8*, 506.
[250] A. Yang, T. B. Hoang, M. Dridi, C. Deeb, M. H. Mikkelsen, G. C. Schatz, T. W. Odom, *Nat. Commun.* **2015**, *6*, 6939.
[251] A. Yang, Z. Li, M. P. Knudson, A. J. Hryn, W. Wang, K. Aydin, T. W. Odom, *ACS Nano* **2015**, *9*, 11582.
[252] W. Wang, M. Ramezani, A. I. Väkeväinen, P. Törmä, J. G. Rivas, T. W. Odom, *Mater. Today* **2018**, *21*, 303.
[253] T. K. Hakala, H. T. Rekola, A. I. Väkeväinen, J. P. Martikainen, M. Nečada, A. J. Moilanen, P. Törmä, *Nat. Commun.* **2017**, *8*, 13687.
[254] R. Guo, M. Nečada, T. K. Hakala, A. I. Väkeväinen, P. Törmä, *Phys. Rev. Lett.* **2019**, *122*, 013901.
[255] A. Fernandez-Bravo, D. Wang, E. S. Barnard, A. Teitelboim, C. Tajon, J. Guan, G. C. Schatz, B. E. Cohen, E. M. Chan, P. J. Schuck, T. W. Odom, *Nat. Mater.* **2019**, *18*, 1172.
[256] S. I. Azzam, V. M. Shalaev, A. Boltasseva, A. V. Kildishev, *Phys. Rev. Lett.* **2018**, *121*, 253901.
[257] Y. Wang, L. Zhou, Y. Zhang, J. Yu, B. Huang, Y. Wang, Y. Lai, S. Zhu, J. Zhu, *Adv. Opt. Mater.* **2018**, *6*, 1800813.
[258] M. Qin, L. Wang, X. Zhai, D. Chen, S. Xia, *Nanoscale Res. Lett.* **2017**, *12*, 578.
[259] T. Braun, V. Baumann, O. Iff, S. Höfling, C. Schneider, M. Kamp, *Appl. Phys. Lett.* **2015**, *106*, 041113.
[260] Y. D. Shah, J. Grant, D. Hao, M. Kenney, V. Pusino, D. R. S. Cumming, *ACS Photonics* **2018**, *5*, 663.
[261] A. M. Lakhani, M.-k. Kim, E. K. Lau, M. C. Wu, *Opt. Express* **2011**, *19*, 18237.

Baoqing Wang is currently a Ph.D. researcher in the group of Prof. Zhiming Wang in the Institute of Fundamental and Frontier Sciences of the University of Electronic Science and Technology of China. He received the B.S. degree in Materials Engineering in 2016. His current research is focusing on plasmonic devices.

Peng Yu is currently a research assistant in the Institute of Fundamental and Frontier Sciences of the University of Electronic Science and Technology of China. He obtained his bachelor's degree in Microelectronics in 2012, master's degree in 2015, and Ph.D. degree in 2018. His current research interests include plasmon-enhanced light–matter interactions, photonic integrated circuits.

Zhiming M. Wang is currently a professor in the Institute of Fundamental and Frontier Sciences of the University of Electronic Science and Technology of China. He obtained his bachelor's degree in Applied Physics in 1992, master's degree in Semiconductor Physics in 1995, and his Ph.D. degree in Condensed Matter Physics in 1998. He did postdoctoral studies in Paul-Drude-Institute for Solid-State Electronics, Berlin, Germany, in 2000. His current research interests focus on epitaxial crystal growth, quantum dots, surfaces, interfaces, and plasmonics.